AGU PUBLICATIONS

JGR

Journal of Geophysical Research: Oceans

RESEARCH ARTICLE

10.1002/2016JC012634

Special Section:

Dense Water Formations in the North Western Mediterranean: From the Physical Forcings to the Biogeochemical Consequences

Key Points:

- A submesoscale coherent vortex is characterized using shipborne measurements (CTD and water samples) combined with glider data
- The eddy is very nonlinear with vorticity reaching $-0.8f$ and coherent with a diffusive half-life of about 2.5 year
- The eddy is nutrient-depleted at depth, but enhances phytoplankton growth (especially microphytoplankton) as well as primary production

Correspondence to:

A. Bosse,
anthony.bosse@uib.no

Citation:

Bosse, A. et al. (2017), A submesoscale coherent vortex in the Ligurian Sea: From dynamical barriers to biological implications, *J. Geophys. Res. Oceans*, *122*, 6196–6217, doi:10.1002/2016JC012634.

Received 15 DEC 2016
Accepted 28 APR 2017
Accepted article online 4 MAY 2017
Published online 3 AUG 2017

A submesoscale coherent vortex in the Ligurian Sea: From dynamical barriers to biological implications

Anthony Bosse[1,2], Pierre Testor[2], Nicolas Mayot[3], Louis Prieur[3], Fabrizio D'Ortenzio[3], Laurent Mortier[2,4], Hervé Le Goff[2], Claire Gourcuff[2,5], Laurent Coppola[3], Héloïse Lavigne[6], and Patrick Raimbault[7]

[1]Bjerknes Center for Climate Research, Geophysical Institute, University of Bergen, Bergen, Norway, [2]Laboratoire LOCEAN, Sorbonne Universités (UPMC, Université Paris 06)-CNRS-IRD-MNHN, Paris, France, [3]Laboratoire d'Océanographie de Villefranche, Sorbonne Universités (UPMC, Université Paris 06)-CNRS, Villefranche/mer, France, [4]ENSTA Paristech, Palaiseau, France, [5]Euro-Argo ERIC, Brest, France, [6]Istituto Nazionale di Oceanografia e di Geofisica Sperimentale, Trieste, Italy, [7]Aix-Marseille University, Sud Toulon-Var University, CNRS/INSU, IRD, MIO, Marseille, France

Abstract In June 2013, a glider equipped with oxygen and fluorescence sensors has been used to extensively sample an anticyclonic Submesoscale Coherent Vortex (SCV) in the Ligurian Sea (NW Mediterranean Sea). Those measurements are complemented by full-depth CTD casts (T, S, and oxygen) and water samples documenting nutrients and phytoplankton pigments within the SCV and outside. The SCV has a very homogeneous core of oxygenated waters between 300 and 1200 m formed 4.5 months earlier during the winter deep convection event. It has a strong dynamical signature with peak velocities at 700 m depth of 13.9 cm s^{-1} in cyclogeostrophic balance. The eddy has a small radius of 6.2 km corresponding to high Rossby number of -0.45. The vorticity at the eddy center reaches $-0.8f$. Cross-stream isopycnic diffusion of tracers between the eddy core and the surroundings is found to be very limited due to dynamical barriers set by the SCV associated with a diffusivity coefficient of about 0.2 m^2 s^{-1}. The deep core is nutrients-depleted with concentrations of nitrate, phosphate, and silicate, 13–18% lower than the rich surrounding waters. However, the nutriclines are shifted of about 20–50 m toward the surface thus increasing the nutrients availability for phytoplankton. Chlorophyll-a concentrations at the deep chlorophyll maximum are subsequently about twice bigger as compared to outside. Pigments further reveal the predominance of nanophytoplankton inside the eddy and an enhancement of the primary productivity. This study demonstrates the important impact of postconvective SCVs on nutrients distribution and phytoplankton community, as well as on the subsequent primary production and carbon sequestration.

Plain Language Summary Due to harsh meteorological conditions in winter, a few places of the world's ocean experience an intense cooling of their surface waters that start to sink in a process called oceanic deep convection. It is crucial for the functioning of the ocean, but also the marine biology as it brings oxygen deep below the surface and nutrients up to the surface thereby stimulating phytoplankton growth. In this study, we describe with unprecedented details the physics and its biological implications of an eddy formed after a convective event occurring in winter 2013 south of France in the northwestern Mediterranean Sea. This oceanic eddy has a radius of about 6 km and a subsurface signature with intensified rotation of about 15 cm/s at around 750 m. Its size is rather small for an oceanic eddy and makes it particularly challenging to sample and detect. This type of eddies are able to live for years in the quiescent deep ocean and this specimen was observed 4.5 months after its formation. Water samples collected by a ship inside the eddy enable us to further evaluate for the first time its influence on the nutrients concentration, as well as on the phytoplankton size group.

1. Introduction

The northwestern Mediterranean Sea is one the few particular places of the world's oceans, where intense atmospheric forcing combined to a weak ocean stratification allows vertical mixing to reach depths (>1500–2000 m). This phenomenon is called open-ocean deep convection and is of critical importance for the ventilation of the deep oceans and has been studied since the 1970s (see *Marshall and Schott* [1999] for a review). It can be divided into three main phases (that however overlap in space and time) [*MEDOC-Group*, 1970]: *the preconditioning* consisting in a basin-scale cyclonic circulation causing a doming of isopycnals at its center; *the mixing phase*, which results from cold and dry winds blowing over the preconditioned area leading to intense heat losses of the ocean and a deepening of the mixed layer (typically several hundreds of watts per square meter for a couple of days [*Leaman and Schott*, 1991]); the *spreading phase* induced by the restratification of the water column that occurs, when the intense heat losses cease (generally in early spring). During this last phase, the mixed patch of convected waters breaks up into numerous eddies by conversion of potential energy into kinetic energy through baroclinic instability [*Gascard*, 1978; *Legg and Marshall*, 1993; *Visbeck et al*., 1996; *Jones and Marshall*, 1997]. In particular, submesoscale coherent vortices are formed [*McWilliams*, 1985]. They are characterized by a small radius, subsurface peak velocities, and an extended lifetime (>1 year). They were found to be involved in the large-scale spreading of newly formed deep waters toward the western Mediterranean Sea [*Testor and Gascard*, 2003, 2006], the Greenland Sea [*Gascard et al*., 2002], and the Labrador Sea [*Lilly and Rhines*, 2002]. In the western Mediterranean Sea, this process has been recognized as being particularly important: SCVs could transport 30–50% of the newly formed deep waters out of the convective zone [*Testor and Gascard*, 2006; *Bosse et al*., 2016; *Damien et al*., 2017], while another important part could be transported by the mean circulation [*Send et al*., 1996].

The strong rotation of SCVs sets transport barriers at that drastically reduce the lateral exchanges between their deep core and the surrounding waters [*Rhines and Young*, 1983; *Provenzale*, 1999]. As a consequence, they are therefore extremely efficient in transporting physical and biogeochemical tracers characteristics of their generation site over long distances [*D'Asaro*, 1988; *Testor and Gascard*, 2003; *Bower et al*., 2013]. As a consequence, they can greatly impact the biogeochemical cycles at a local scale. For instance, *Budéus et al*. [2004] reported a significant increase in the bacteria abundance at great depths within deep SCVs observed in the Greenland Sea. *Durrieu de Madron et al*. [2017] reveal sediments being trapped within cyclonic SCVs in the NW Mediterranean Sea. In oxygen-depleted oceans, they have been identified as local spots for denitrification [*Löscher et al*., 2015; *Karstensen et al*., 2017] and habitat compression due to their very low oxygen content [*Lachkar et al*., 2016]. Especially in tropical oceanic basins, subsurface eddies can be tentatively be detected from space when combined with infrared satellite images [*Klemas and Yan*, 2014], even though the surface expression of deep subsurface eddies is often small [*Ciani et al*., 2015]. In the Mediterranean Sea, as well as in high-latitude environment characterized by small deformation radii of 5–10 km, sampling the fine scale of eddies remnant of wintertime convection is thus very challenging.

By allowing a relatively high horizontal resolution (distance between consecutive profiles 2–4 km), autonomous gliders could characterize the dynamics of postconvective SCVs of about 10 km in diameter observed in the NW Mediterranean Sea [*Bosse et al*., 2016]. Winter 2013 was an intense convective year that produced many vertical structures. In this study, we analyze in situ observations collected during summer 2013 in the Ligurian Sea by a research vessel and a glider in the same SCV. About 10 days after the first survey by the R/V, the glider met by pure luck the same eddy around 30 km to the southwest from the first observation. Both observations have very high similarities in their vertical structure and are separated by a relative close distance in space and time in coherence with the typical drift of SCVs. The intense sampling of the upper 1000 m by the glider combined with full-depth CTD casts and water samples documenting the nutrients concentrations, as well as phytoplankton pigments, enables the first detailed study of such a small-scale postconvective vortex.

2. Data and Methods

2.1. Basin-Scale Cruise

Since 2010, sustained observations of the circulation and water properties are carried out within the framework of the MOOSE project (NW Mediterranean Sea Observatory, http://www.moose-network.fr/). The MOOSE-GE cruises aim at providing a yearly snapshot in summer of the open-ocean part of the basin with about 70–100 CTD stations. As an important part of this integrated ocean observing system, gliders are also regularly deployed in the whole subbasin along repeated sections. The common key objective of the MOOSE observatory is to monitor the deep waters formation in the Gulf of Lions in order to assess its effect

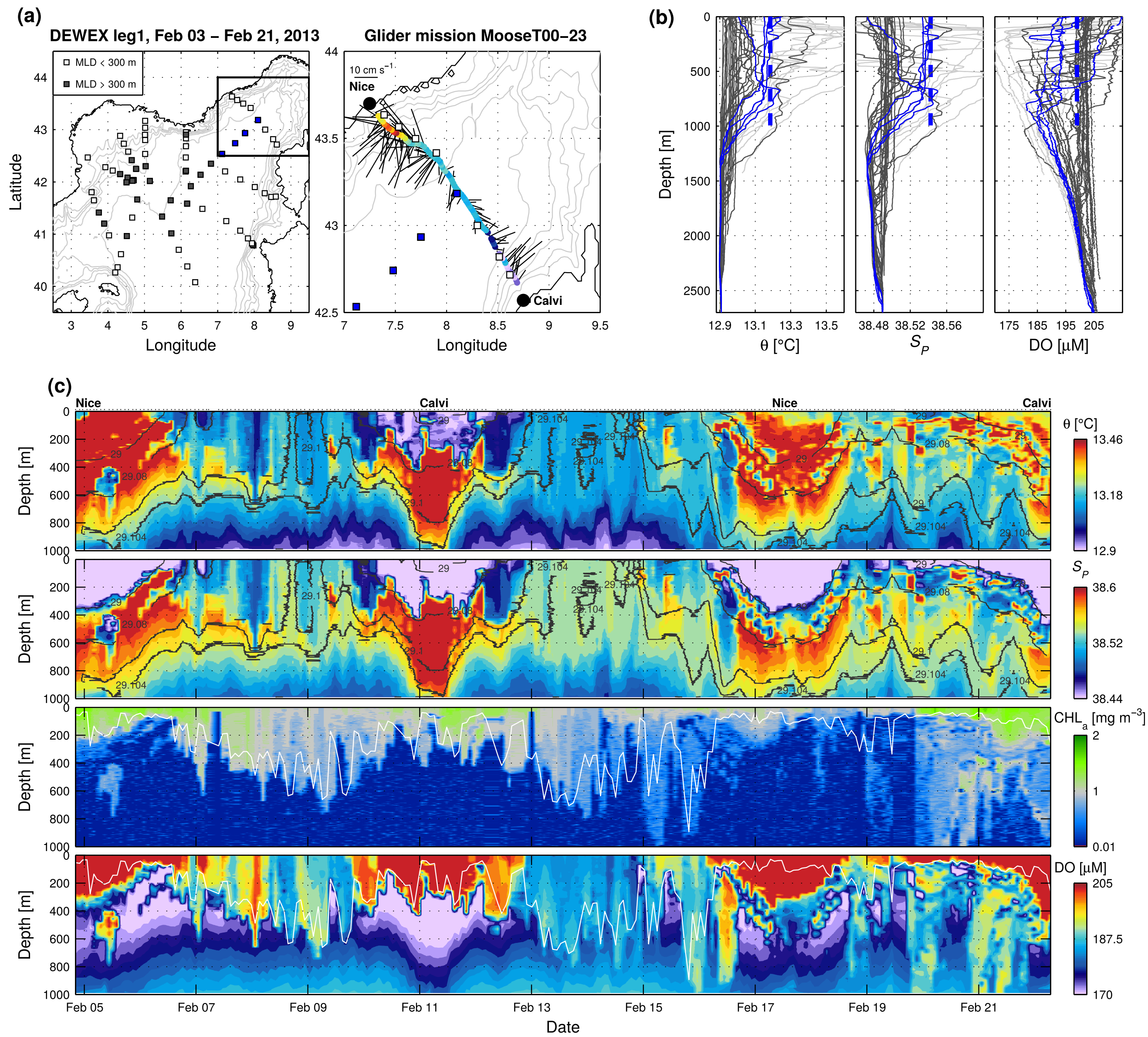

Figure 1. (a) CTD casts carried out in the Ligurian Sea during the DEWEX winter cruise in February 2013. Stations were distinguished according to the observed mixed-layer depth. The right figure shows the trajectory of glider during the concomitant glider mission MOOSE T00-23. Dots are colored according to the mixed-layer mean potential temperature observed between 11 and 17 February with the same color scale as in Figure 1c. Depth-average currents estimated by the glider are also shown in dark gray. (b) Full-depth shipborne CTD casts during the winter with dark gray profiles corresponding to deeply mixed profiles. The blue profile is a deeply mixed profile carried out in the Ligurian Sea. The SCV core characteristics are indicated by the thick dashed blue line. (c) Glider section along three consecutive Nice-Calvi sections. (top–bottom) Potential temperature, practical salinity, chlorophyll-a fluorescence, and dissolved oxygen. Black contours are isopycnals and the white line represents the mixed-layer depth. On top of these panels, dots show the high-resolution sampling of the glider.

on biogeochemical cycles and on the longer-term environmental and ecosystemic trends and anomalies [*Durrieu de Madron et al.*, 2011].

The period 2012–2013 was a period of particular intense sampling with six basin-scale surveys from July 2012 to September 2013 [*Estournel et al.*, 2016; *Testor et al.*, 2017].

2.1.1. Hydrographical Data

In February 2013, the DEWEX leg 1 was carried out in the NW Mediterranean Sea [*Testor*, 2013]. With 75 CTD casts distributed over the whole basin, it enables to get a precious picture of the winter deep convection at its climax (see Figure 1). In June–July 2013, 72 CTD stations have been collected during the MOOSE-GE 2013

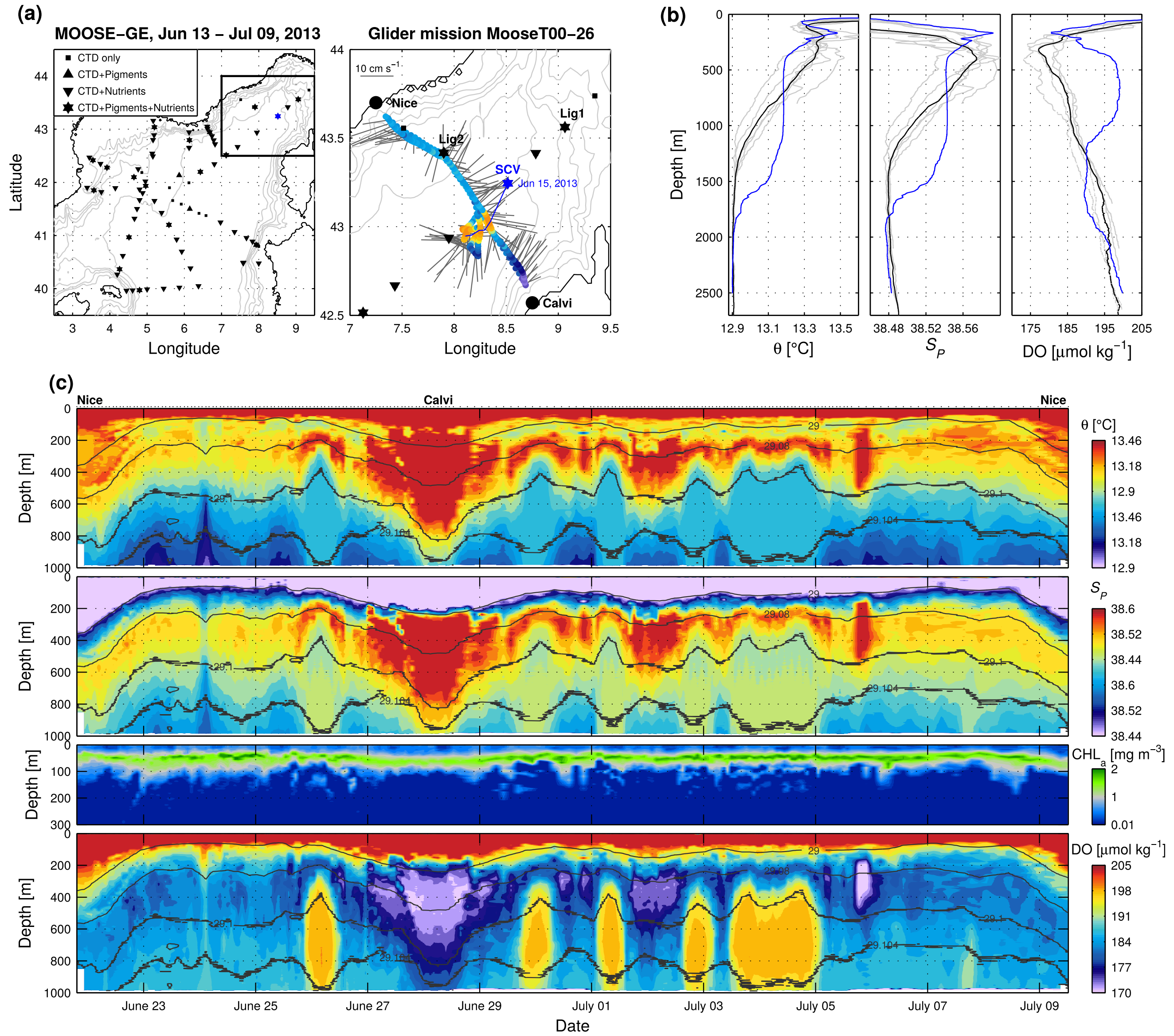

Figure 2. Same as Figure 1 but for the MOOSE-GE 2013 summer cruise and the MOOSE T00-25 glider mission carried out in June–July 2013. In Figure 2a, the colored dots along the glider trajectory represents the dissolved oxygen concentration with the same scale as in Figure 2c. Note that total carbon was measured at the same stations as phytoplankton pigments. In Figure 2b, the light gray profiles correspond to those carried out in the Ligurian Sea (defined by the black box drawn in Figure 2a), the black profile is the average of all the gray profiles. The blue profile was carried out within the core of a deep eddy that was further sampled by a glider shortly afterward.

cruise [*Testor et al*., 2013]. A profile revealed the presence of a subsurface vortex in the Ligurian Sea (see Figure 2). The conductivity, temperature, and pressure measurements during those two cruises have been performed using a Seabird SBE911+ CTD probe. The CT sensors have been calibrated by predeployment and postdeployment laboratory analysis. After calibration, the absolute accuracy of the measurements is 0.003 for the salinity and 0.001°C for the temperature. These calibrated CTD casts provide a ground truth for the autonomous underwater gliders.

2.1.2. Lowered ADCP (LADCP)

During the MOOSE-GE 2013 cruise, the rosette was carrying two RDI WH 300 kHz LADCPs (up and down looking). Sixty-one LADCP profiles were processed with the LDEO V8b code based on the inversion method developed by *Visbeck* [2002]. All profiles were inversed at 8 m vertical resolution using both instruments from the surface to the bottom, navigation data from the CTD file, and bottom track constraint when available. Precision on horizontal velocities ranges from 2 to 4 cm s^{-1} for all validated profiles. Here we use the LADCP profile carried within the eddy (leg 1, station 7).

2.1.3. Dissolved Oxygen

The rosette was equipped with a SBE43 sensor for dissolved oxygen (DO), which has been calibrated before the cruises operation and after with postcruises manufacturer calibrations. After calibration, the absolute accuracy of the measurements is about 5 μmol kg^{-1}. In addition, Winkler titration has been performed on board after seawater sampling. The measurements have been done each day (every four to five stations) and the SBE43 sensor has been cleaned after each CTD cast following the manufacturer recommendations [*Janzen et al.*, 2007]. Later on, the Winkler analysis has been used to adjust the SBE43 raw data, as specified by the GO-SHIP group (http://www.go-ship.org/).

2.1.4. Nutrients

Water samples for nitrate, nitrite, phosphate, and silicic acid determination were collected from the Niskin bottles into 20 mL polyethylene flasks and immediately poisoned with 10 μg L^{-1} mercuric chloride and stored for subsequent laboratory analysis following *Kirkwood* [1992]. Nitrate (NO_3^-), phosphate (PO_4^{3-}), and silicate ($Si(OH)_4$) ions were analyzed in laboratory by standard automated colorimetric system using a Seal Analytical continuous flow AutoAnalyser III according to *Aminot and Kérouel* [2007]. In-house standards regularly compared to the commercially available products (OSIL) were used to ensure the reproducibility of the measurements between the analyses.

2.1.5. Dissolved Inorganic Carbon

For C_T (or DIC) measurements, seawater samples were collected into washed 500 mL borosilicate glass bottles, and poisoned with a saturated solution of $HgCl_2$. At the end of the cruise, the samples were sent to the SNAPO (Service National d'Analyse des Paramêtres Océaniques du CO_2, http://soon.ipsl.jussieu.fr/SNAPOCO2/) for analysis. The measurements were performed by potentiometric titration using a closed cell, as described in details in the handbook of methods for the analysis of the various parameters of the CO_2 system in seawater [*DOE*, 1994]. The precisions obtained for these measurements are 2.2 μmol kg^{-1}.

2.1.6. Pigments

The vertical distribution of phytoplankton pigment concentrations was determined through discrete water samples collected with Niskin bottles mounted on the CTD rosette. The discrete water samples were then filtered (GF/F) and High-Performance Liquid Chromatography (HPLC) analyses were performed to provide a precise determination of the different phytoplankton pigments concentrations. All HPLC measurements used here were conducted at the Laboratoire dÓcéanographie de Villefranche (see *Ras et al.* [2008] for details on the HPLC method). As in *Mayot et al.* [2017a], we used the pigment-based approach proposed by *Claustre* [1994] and further improved by *Vidussi et al.* [2001] and *Uitz et al.* [2006] to estimate the contribution of three phytoplankton size classes: micro, nano, and picophytoplankton (respectively, f_{micro}, f_{nano}, and f_{pico}) to the total phytoplankton biomass estimated as $[Chl_a]$ the chlorophyll-a concentration. Seven diagnostic pigments were selected as biomarkers of major phytoplankton taxa: fucoxanthin ($[Fuco]$), peridinin ($[Perid]$), alloxanthin ($[Allo]$), 19′-butanoyloxyfucoxanthin ($[ButFuco]$), 19′-hexanoyloxyfucoxanthin ($[HexFuco]$), zeaxanthin ($[Zea]$), and total chlorophyll-b (chlorophyll-b + divinyl chlorophyll-b = $[TChl_b]$) to compute f_{micro}, f_{nano}, and f_{pico}.

$$f_{micro}=(1.41[Fuco]+1.41[Perid])/\sum DPW, \tag{1}$$

$$f_{nano}=(1.27[HexFuco]+0.35[ButFuco]+0.60[Allo])/\sum DPW, \tag{2}$$

$$f_{pico}=(1.01[TChl_b]+0.86[Zea])/\sum DPW, \tag{3}$$

with $\sum DPW$ a weighted sum of the seven diagnostic pigments concentration: $DPW=(1.41[Fuco]+1.41[Perid]+1.27[HexFuco]+0.35[ButFuco]+0.60[Allo]+1.01[TChl_b]+0.86[Zea])$. Eventually, the phytoplankton class-specific vertical profiles of chlorophyll-a were deduced by $[Chl_a]_{class}(z)=[Chl_a](z)f_{class}(z)$.

2.1.7. Primary Production

The phytoplankton primary production was estimated using the bio-optical model described by *Morel* [1991]. The euphotic depth was determined from vertical profiles of $[Chl_a](z)$ [*Morel and Berthon*, 1989; *Morel and Maritorena*, 2001] and combined with the phytoplankton class-specific photophysiological properties determined by *Uitz et al*. [2008] (see more details in *Mayot et al*. [2017a, supporting information]). The model produces an estimate of the primary production associated with each of the three phytoplankton size classes (P_{micro}, P_{nano}, and P_{pico}).

2.2. Glider Missions

Autonomous oceanic gliders are now an essential part of ocean observing techniques [*Testor et al*., 2010]. They sample the ocean along a saw-tooth trajectory between the surface and 1000 m. The typical slope of isopycnals are much smaller than the pitch angle of the glider (about $\pm$15–25°), so dives and ascents can be considered as vertical profiles and are separated by typically 2–4 km and 2–4 h depending on the sampling strategy (dives only, or dives/ascents). Having a horizontal speed of 30–40 km/d, they are perfectly suited to sample oceanic features like eddies that propagate slower [*Martin et al*., 2009; *Frajka-Williams et al*., 2009; *Bouffard et al*., 2010, 2012; *Fan et al*., 2013; *Pelland et al*., 2013; *Bosse et al*., 2015, 2016; *Cotroneo et al*., 2015; *Thomsen et al*., 2016]. In the framework of the MOOSE project, gliders are deployed on a regular basis and in particular along the Nice-Calvi section crossing the Ligurian Sea [*Bosse et al*., 2015]. Here we use two deployments of Slocum gliders along this endurance line: the mission MOOSE T00–23 in January–March and MOOSE T00–26 in June–July 2013.

2.2.1. Hydrographical Data

The gliders were equipped with an unpumped Seabird SBE41CP CTD probe. Direct comparisons with calibrated shipborne CTD measurements could be done for both deployments following the approach used in *Bosse et al*. [2015, 2016]. For the summer mission (MOOSE T00–26), we refined the calibration by adjusting the glider data on the calibrated CTD inside the SCV core. Given the very homogeneous SCV core, both platforms agree very well: the root mean square (RMS) difference between 600 and 800 m depth inside the SCV of 0.002°C in temperature and 0.001 in salinity, which is comparable with the shipborne CTD accuracy. In addition, thermal lag effects of the probe that can affect salinity measurements in the strong summer thermocline have been corrected following *Garau et al*. [2011].

2.2.2. Depth-Average Currents

From their dead reckoning navigation and GPS fixes made at the surface, gliders deduce a mean current. This latter represents the mean current over each dive and will hereafter be referred as the depth-average currents (DAC). A compass calibration has been carried out before each deployment allowing DAC to be used to reference geostrophic velocities as commonly done (see for instance the previously cited literature).

2.2.3. Dissolved Oxygen

The gliders were equipped with an Anderraa Optode 3835. The raw phase measurements were corrected from a sensor time response estimated by comparing measurements of consecutive up and down profiles. Time delays of 30 s (MOOSE T00–23) and 25 s (MOOSE T00–26) were estimated, the same order of magnitude than the 25 s provided by the manufacturer. Oxygen concentration was then computed using the corrected phase measurements and temperature measurements from the CTD, following the Argo recommendations [*Thierry and Bittig*, 2016]. As a final calibration step, an offset (respectively 10.0 and 20.3 μmol kg^{-1} for the missions MooseT00–23 and T00–26) and a slope (respectively, 0.016 and $-$0.0049 μmol kg^{-1} m^{-1}) were least squares fitted in order to minimize the difference between the glider optode and calibrated shipborne measurements. The comparison is made with CTD casts carried out at less than 50 km and 2 days apart from glider measurements for the winter mission and with profiles carried out in the SCV core for the summer deployment. After this calibration procedure, the RMS difference between the glider and shipborne measurements at depth was, respectively, 1.5 and 1.3 μmol kg^{-1}, which is below the accuracy of absolute shipborne measurement.

2.2.4. Chl-*a* Fluorescence

The glider also had a Wet Labs bio-optical fluorometer. Unfortunately, no direct comparison with HPLC measurements was possible with the glider data, as the short response time of phytoplankton growth imposes a very close match-up in space and time. Alternatively, a calibration method using satellite ocean color was applied [*Lavigne et al*., 2012]. In this calibration step, fluorescence profiles were also corrected for nonphotochemical quenching following *Xing et al*. [2012]. With a larger data set, *Mayot et al*. [2017b] tested this method against bottle measurements. Both calibrations gave satisfying and similar results (mean absolute deviation percent of 23% with HPLC and 38% with satellite), thus supporting the use of the method of *Lavigne et al*. [2012] when direct comparison with in situ data is not possible.

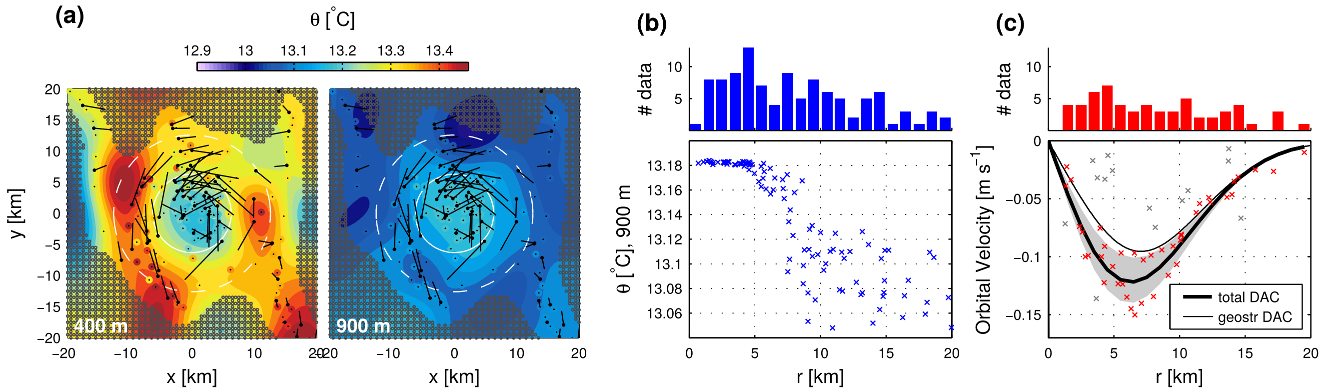

Figure 3. Glider sampling of the SCV. (a) Optimal interpolation of the potential temperature at 400 and 900 m in the eddy centered rotating coordinate framework (i.e., all profiles and depth-average currents from the glider have been rotated around the eddy center according to radial orbital depth-average currents and their observation date). Radial distribution of (b) potential temperature at 900 m and (c) orbital depth-average currents estimated by the glider. The fitted Gaussian distribution of orbital velocities is also drawn (r_0=6.3 km and v_0= 12.2 cm s^{-1}). The geostrophic component of orbital depth-average currents deduced following *Bosse et al*. [2016] is also shown by the light black line. Note that outliers plotted in gray have been excluded prior to the curve fitting. Histograms representing the number of observations in 1 km bins are also shown in top figures.

2.3. Remote Sensing

Surface chlorophyll concentration from level 2 MODIS Aqua product (daily and at 1 km resolution) was extracted over the northwestern Mediterranean Sea from the NASA web site (http://oceancolor.gsfc.nasa.gov/). All the MODIS L2 flags have been applied.

2.4. SCV Reconstruction

2.4.1. Vortex Center Detection

As in *Bosse et al*. [2015, 2016], glider depth-average currents are used to retrieve the eddy velocity field. A mean advection is estimated by low-passing the along-track DAC using a Gaussian moving average of 35 km variance. The eddy center detection method is then applied on the DAC minus the local advection. In order to find the eddy center, the following cost function is minimized: $g(x,y)=1/n\sum_{i=1}^{n}[\mathbf{v_i}\cdot\mathbf{r_i}(x,y)/||\mathbf{r_i}(x,y)||]^2$ with (*x*, *y*) a given position in the horizontal plane, $\mathbf{r_i}(x,y)/||\mathbf{r_i}(x,y)||$ the normalized vector linking (*x*, *y*) to the location where the depth-average velocities $\mathbf{v_i}$ are estimated. We choose $n=4$ centered around each vortex center to preserve the synoptic character of the sampling [see *Bosse et al*., 2015, Figure 7] for an illustration of this cost function method).

The SCV center is thus detected five times from 26 June to 4 July 2013 (see Figure 2c). During that time period, 106 glider profiles and 59 DACs were carried out at less than 20 km of the eddy center. Every profile could then be positioned in the eddy coordinate framework in order to reconstruct its dynamics (see Figure 3).

2.4.2. Objective Mapping

Full-depth shipborne CTD cast were collected inside the eddy core and outside (see Figure 2). Those profiles provide useful information below 1000 m, the maximum sampling depth of the glider. In order to map the eddy properties (θ, S_P, and DO) down to the seafloor at about 2500 m, an objective mapping was performed with a spatial decorrelation scale of 6.3 km in the radial and 800 m in the vertical axis (see Figure 4) [*Bretherton et al*., 1976; *Le Traon*, 1990]. This radial scale results from the eddy radius deduced from the DACs (see caption of Figure 3c) and the vertical scale corresponds to the thickness of the homogeneous core. To perform this analysis, we used all the glider profiles in the top 1000 m and only two full-depth shipborne profiles below. The shipborne CTD cast within the core was positioned at $r=3.8$ km from the eddy center by fitting the mean LADCP velocity of the 0–1000 m layer (11.0 cm s^{-1}) to the glider DACs (see Figure 3c). And the profile representative of the background, taken as the mean profile observed in the Ligurian Sea during the MOOSE-GE cruise (see Figure 2b), was positioned at $r=20$ km (more than three eddy radius).

Objective mapping of potential temperature was also performed in the horizontal plane and in the eddy coordinate system (see Figure 3a). For these interpolations, an isotropic decorrelation scale of 6.3 km has simply been used.

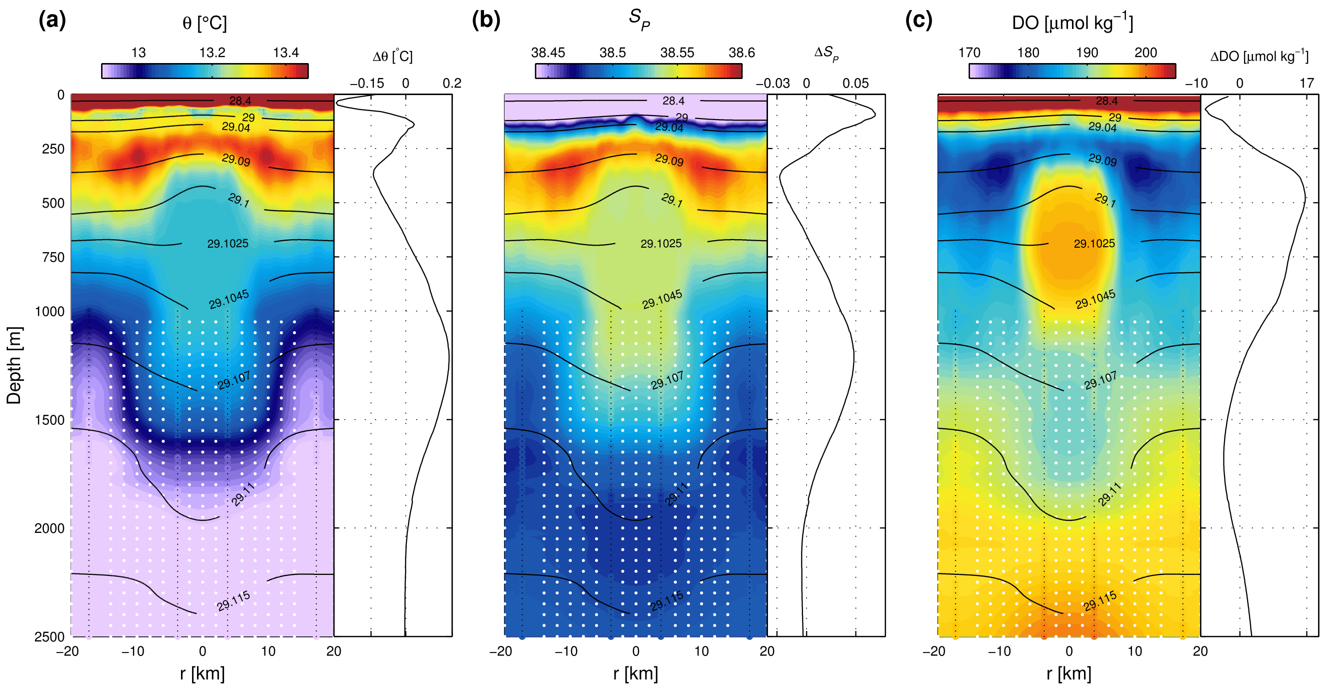

Figure 4. Hydrography of the SCV. Radial distribution of (a) potential temperature, (b) practical salinity, and (c) dissolved oxygen (DO). Black contours represent potential density in kg m^{-3}. All those fields result from the optimal interpolation constrained by the intense glider survey of the first 1000 m depth. Below that depth, area away from the full-depth profiles inside and outside the SCV core has been shaded. Those profiles are also shown as scatter points on top of the analyzed fields. Note that a radial symmetry has been applied for aesthetic and clarity purposes.

2.4.3. Eddy Dynamics in Gradient Wind Balance

Small-scale vortices are generally characterized by a relatively strong horizontal shear ($>0.1f$). Their force balance are thus ageostrophic and the centrifugal force needs to be taken into account; otherwise, the velocity are underestimated for anticyclones and overestimated for cyclones [*Elliott and Sanford*, 1986; *Penven et al.*, 2014; *Bosse et al.*, 2015, 2016]. The cyclostrophic velocities v_c can be retrieved by solving the quadratic equation expressing the gradient wind balance in a cylindrical coordinate system: $v_c^2(r,z)/r+fv_c(r,z)=fv_g(r,z)$ with r the distance to the eddy center, z the depth, f the Coriolis parameter, and v_g the geostrophic velocity field. Keeping the relevant solution from this equation then yields,

$$v_c(r,z)=\frac{rf}{2}\left(-1+\sqrt{1+\frac{4v_g(r,z)}{rf}}\right). \tag{4}$$

The negative root of the quadratic equation is excluded as it corresponds to nonstable solutions with vorticity below $-f$. Note that this equation can be solved only if the geostrophic shear is not too strongly anticyclonic (i.e., $4v_g(r,z)/rf<-1$). As expected, the amplitude of cyclogeostrophic velocities are smaller (respectively larger) than v_g for cyclones (respectively anticyclones). To infer cyclostrophic velocities, absolute geostrophic velocities have thus to be determined first.

Classically, the cross-track geostrophic vertical shear is computed by integrating the thermal wind balance from a smoothed density section. Here we applied a Gaussian moving average of 3.2 km variance (half of the eddy radius) to the analyzed density field to filter out residual small-scale isopycnals variability without fading the SCV signature. The cutoff length scale is set in accordance with the vortex radius. A modal decomposition on typical density profiles consistently yields a first baroclinic deformation radius of about 6 km. This is relatively small compared to other oceans owing to the low stratification of the northwestern Mediterranean Sea.

For a Gaussian geopotential anomaly, the orbital velocities of the SCV can be written as $V(r)=V_0\frac{r}{r_0}e^{-[(\frac{r}{r_0})^2-1]/2}$, where V_0 corresponds to the velocity maximum located at the distance r_0 from the center [*McWilliams*, 1985; *Pingree and Le Cann*, 1993]. We performed a least squares fit of this Gaussian model to the total DAC from the glider in order to estimate V_0 ($=12.2\pm2.2$ cm s^{-1}) and r_0 ($=6.3\pm0.2$ km).

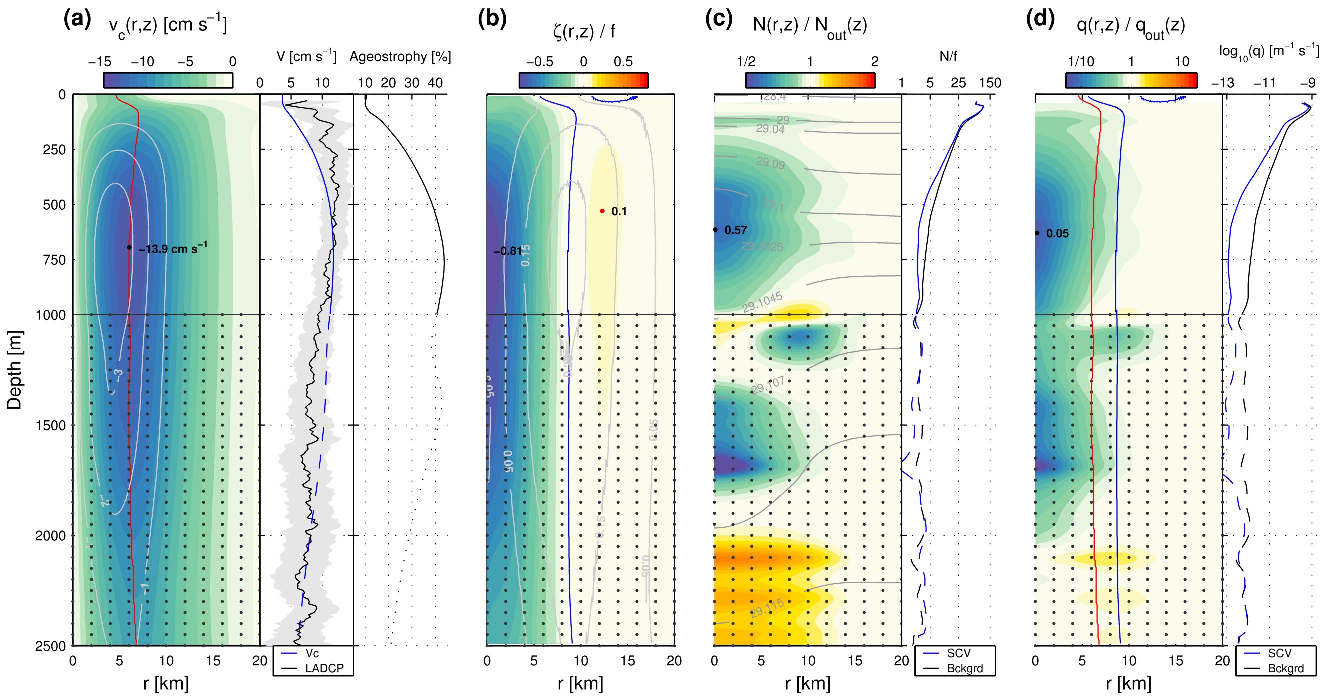

Figure 5. Dynamical diagnostics of the SCV. (a) Radial distribution of cyclogeostrophic velocities v_c. The peak orbital velocity is indicated (at $r = 6.1$ km and 700 m depth). Gray contours represent the only cyclostrophic component of orbital velocities. The red line follows peak velocities over depth. The right figure quantifies the ageostrophy percentage over depth: $(1-max_z|v_g|/max_z|v_c|)\times 100$. (b) Relative vorticity normalized by *f*. The blue line follows the change of sign of the vorticity. The minimum and maximum values are also indicated. The gray lines are contours of strain normalized by *f*. (c) Radial distribution of the stratification anomaly relative to the background. The gray contours show the smoothed density field used to compute the geostrophic shear and stratification. (d) Radial distribution of the potential vorticity anomaly relative to the background. The red and blue lines are redrawn on this panel. For Figures 5c and 5d, the background is defined as the averaged field between 15 and 20 km (see black lines in right panels). In contrast, profile representative of the SCV core is taken as the averaged field between 0 and 5 km (see blue lines in right figures). Note that we have shaded the area below 1000 m depth, as dynamical diagnostics are only constrained by two full-depth CTD casts and a subsequent optimal interpolation.

Observations and parameterized velocity show a good agreement with velocities decreasing close to zero within about three radii (see Figure 3b).

Then, the geostrophic component of total depth-average currents is computed following *Bosse et al.* [2016], so the geostrophic shear can be correctly referenced from the surface to 1000 m depth (see details in Appendix A of the latter reference). This method applies when ageostrophy is due to the centrifugal force, which is particularly relevant for small-scale SCVs. The geostrophic component is about 20% smaller in magnitude than total ones (9.8 versus 12.2 cm s^{-1}).

And finally, cyclostrophic velocities are inferred using (4). If the geostrophic shear is directly referenced without removing the cyclostrophic component, the geostrophic shear becomes too intense for equation (4) to be solved (i.e., $4v_g(r,z)/rf < -1$).

Note that isopycnal slope below 1000 m is constrained by only two profiles, one representative of the core and the other of the background. Subsequent errors in the eddy velocity field can thus be the result of miscalculating geostrophic shear. The velocity field shown in Figure 5a still falls into the confidence range of LADCP measurements over the whole water column. They seem to be slightly underestimated close to the surface. The RMS difference is 1.9 cm s^{-1}, which is satisfactory smaller than the LADCP accuracy (mean error of 3.1 cm s^{-1} in velocity amplitude).

2.4.4. Complementary Diagnostics

2.4.4.1. Vorticity, Strain

We computed the relative vorticity from the radial distribution of cyclogeostrophic velocities $v_c(r,z)$: $\zeta(r,z)=\nabla\times\mathbf{v}(r,z)=r^{-1}\partial_r(rv_c)=v_c/r+\partial_r v_c$, as well as the strain rate: $\eta(r,z)=\partial_r v_c-v_c/r$. It expresses the rate at which adjacent fluid parcels will separate under the action of the flow.

2.4.4.2. Potential Vorticity

The Ertel's Potential Vorticity (PV, in m^{-1} s^{-1}) is $q\equiv-\zeta_a\cdot\nabla\sigma/\rho_0$, where $\zeta_a=(\zeta+f)\hat{z}$ is the absolute vorticity. In the ocean interior (i.e., away from surface and bottom boundaries), the fluid is governed by the inviscid

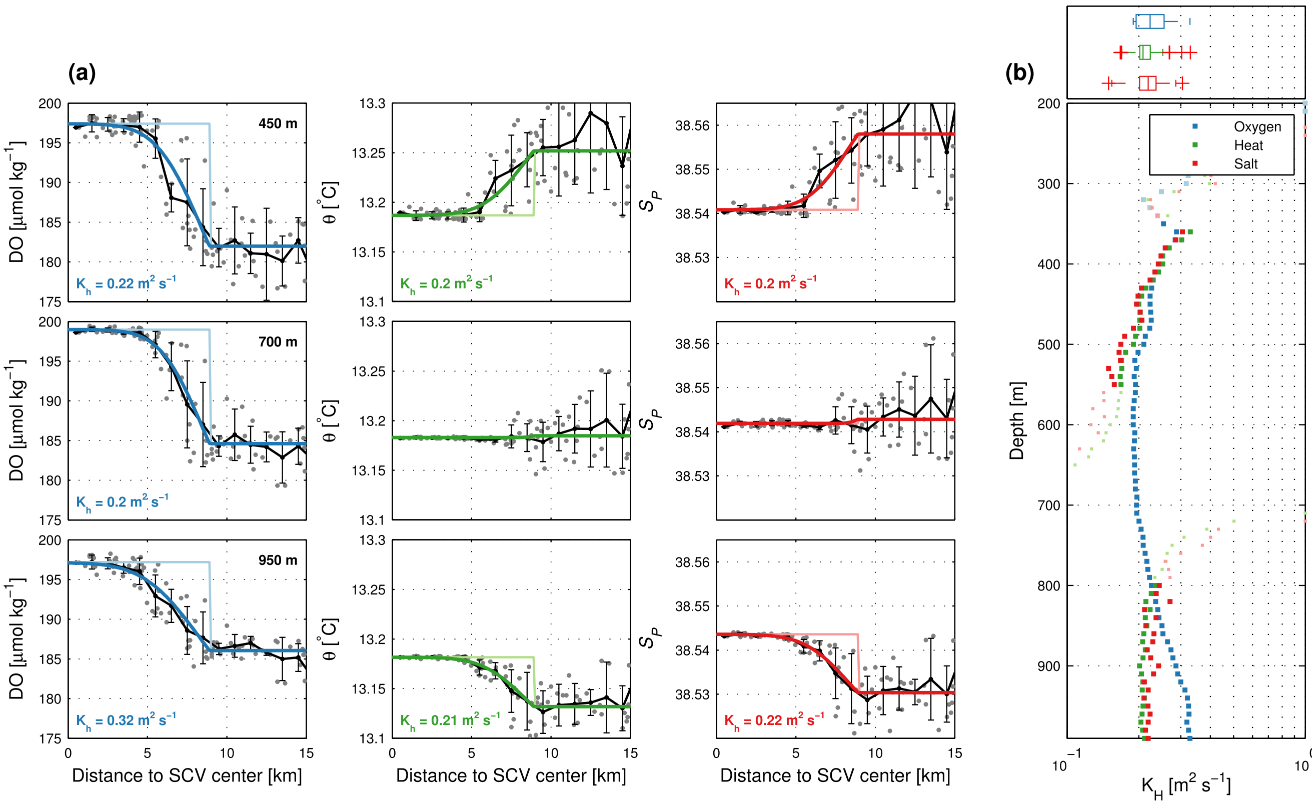

Figure 6. Horizontal diffusion of oxygen, heat, and salt at the rim of the SCV. (a) The gray dots are the individual observations from the glider of dissolved oxygen (left), potential temperature (middle), and salinity (right) at different depths (450, 700, and 950 m, from the top to the bottom). The black line is the average in 1 km bins with error bar showing the standard deviation in each bin. The light colored line represents the tracer distribution at $t=0$ and the thick line after 4.5 months of diffusion with the diffusion coefficient optimized to fit the observed data. (b) Distribution of diffusion coefficient as a function of depth for the different tracers.

Boussinesq equations and this quantity is conservatively advected [*Ertel*, 1942]. In nonfrontal regions where lateral density gradients are small, the PV can be written as, $q(r,z)=fN(r,z)^2(1+Ro(r,z))/g$.

2.5. Lateral Isopycnic Diffusion

The glider collected a remarkable number of profiles (106 at less than 20 km of the center). The glider has sampled the SCV for about 10 days, which is certainly not long enough to measure an evolution of its core. Nonetheless, as we have a good estimate of its age, a lateral eddy diffusion coefficient K_ρ can be fitted to the radial distribution of tracers observed along isopycnals across the eddy core. We assume a step-like initial tracer distribution and then solve the diffusion equation in cylindrical coordinates (details are given in Appendix A). This model describes the evolution under radial diffusion of a cylinder (radius L) with initial concentration T_0 located in an infinite environment of tracer concentration T_∞. The cylinder (representing the SCV) then progressively looses its anomalous concentration until reaching T_∞.

In order to compute K_ρ, some parameters have to be specified. L the radius of the initial tracer distribution is chosen as $\sqrt{2} \simeq 1.41$ eddy radius. This is where vorticity of a Gaussian vortex changes sign. This is also in good agreement with the observed tracer distribution (see Figure 6a). T_∞ the concentration of the surrounding waters is taken as the average between L and 20 km. T_0 is optimized along with K_ρ in order for the theoretical profile to fit to observations. By doing this, we allow the tracer concentration to slightly vary at the top and the base of the core, where vertical diffusion can also be at play and would act rather homogeneously within the eddy core.

The analysis is here conducted for θ, S_P, and DO (see Figure 6a). DO can be considered as a passive tracer below the euphotic layer due to the very low biological activity in absence of sunlight. Dissolved oxygen is probably the most suited tracer, as it exhibits important and consistent lateral gradient across the SCV rim, while temperature and salinity gradients vanish close to its equilibrium depth making diffusion estimate

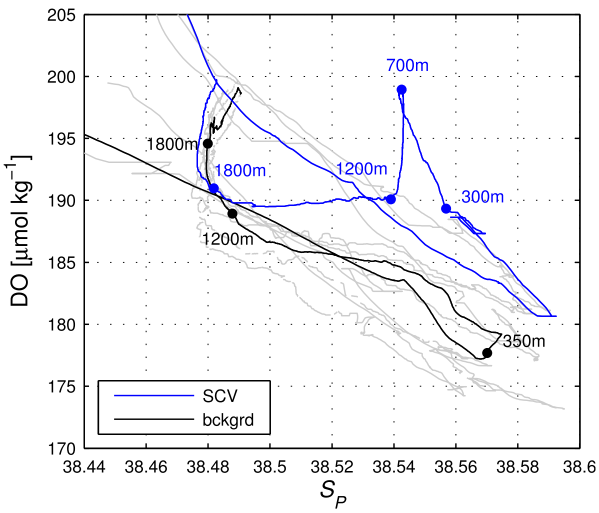

Figure 7. Salinity-oxygen diagram. The gray lines correspond to background profiles carried out in the Ligurian Sea and the black line is their average. The blue line is the particular profile within the SCV.

impossible. However, it remains uncertain if the SCV has an effect on the bacterial activity as shown by *Budéus et al.* [2004]. If it is the case, DO might not be as conservative as it normally is.

2.5.1. Model Validity

Such an approach assumes (1) the vertical diffusion is small compared to horizontal one and (2) the initial distribution is a step. *McWilliams* [1985] gave roughly similar horizontal and vertical diffusivity coefficient for a typical subsurface SCV. Subsequent fluxes should then be mainly controlled by the tracer gradients. The first point is thus valid within the SCV core between 350 and 1000 m, where vertical gradients of tracers are very weak (at least 1 order of magnitude smaller than horizontal ones). The second point is a simplification that would likely cause an overestimation of the diffusivity coefficients. During the dynamical adjustment occurring at the early stage of the SCV's life, sharp gradients will indeed be rapidly smoothed [*McWilliams*, 1988].

3. Results

3.1. Water Mass Transformation During Winter 2013

3.1.1. Basin-Scale Context

There are three main water masses in the Western Mediterranean Sea [*Millot*, 1999]. The fresh (<38.5) and warm (>15°C) Atlantic Waters (AW) found in the surface layers (100–200 m in the basin center and deeper along continental slope due to the boundary circulation, see Figures 1c and 2c). The warm and salty layer of Levantine Intermediate Waters (LIW) was at intermediate depths (200–800 m). This water mass is formed in the Eastern Mediterranean Sea and further spread toward the Western Mediterranean Sea through the Sicily channel. Due to their relatively "old" age, they are characterized by an oxygen minimum when they reach the Western Mediterranean Sea (see Figures 1d and 2d). The Western Mediterranean Deep Waters (WMDW) eventually fill the rest of the water column to the bottom. Due to its relative small overturning timescale, the Mediterranean Sea is highly sensitive to climate change [*Somot et al.*, 2006]. The heat and salt contents of the deep waters have been gradually increasing during the last decades [*Béthoux et al.*, 1990; *Krahmann and Schott*, 1998], with step-like events caused by major deep convection events [*Schroeder et al.*, 2016; *Houpert et al.*, 2016].

In addition to AW, LIW, and WMDW, other less widespread water masses are found. The Winter Intermediate Waters (WIW), which result from intermediate mixing down to about 300 m maximum (above the LIW layer) in open-ocean [*Gasparini et al.*, 2005] or in shelf areas of the Gulf of Lions [*Juza et al.*, 2013] or the Catalan Sea [*Vargas-Yáñez et al.*, 2012]. They are classically characterized by potential temperature below 13°C. Recently, *Bosse et al.* [2016] introduced an additional water mass to complete this picture. Intermediate mixing can indeed result in the episodic formation intermediate waters below the LIW layer at about 500–1000 m depth. This water mass lies deeper than WIW and is also much warmer (>13°C) and saltier (>38.5), as a result of the mixing of the elevated heat and salt contents of the LIW layer. It has been called Winter Deep Waters (WDW). Favorable conditions to its formation were observed in 2012 and 2013 in the Ligurian Sea [*Bosse et al.*, 2016], as well as in 2014 and 2015 in the Gulf of Lions [*Bosse*, 2015].

3.1.2. Winter Mixing in the Ligurian Sea

The glider mission MOOSE T00–23 sampled the Ligurian Sea from January to March at the climax of the deep convection. Figure 1c shows the progressive deepening of the mixed layer (defined using the refined criterion of *Houpert et al.* [2016]). As seen by the glider along the Nice-Calvi section, the mixed layer reaches a maximum depth of about 800 m between 13 and 16 February (see Figure 1c). Shipborne CTD casts were

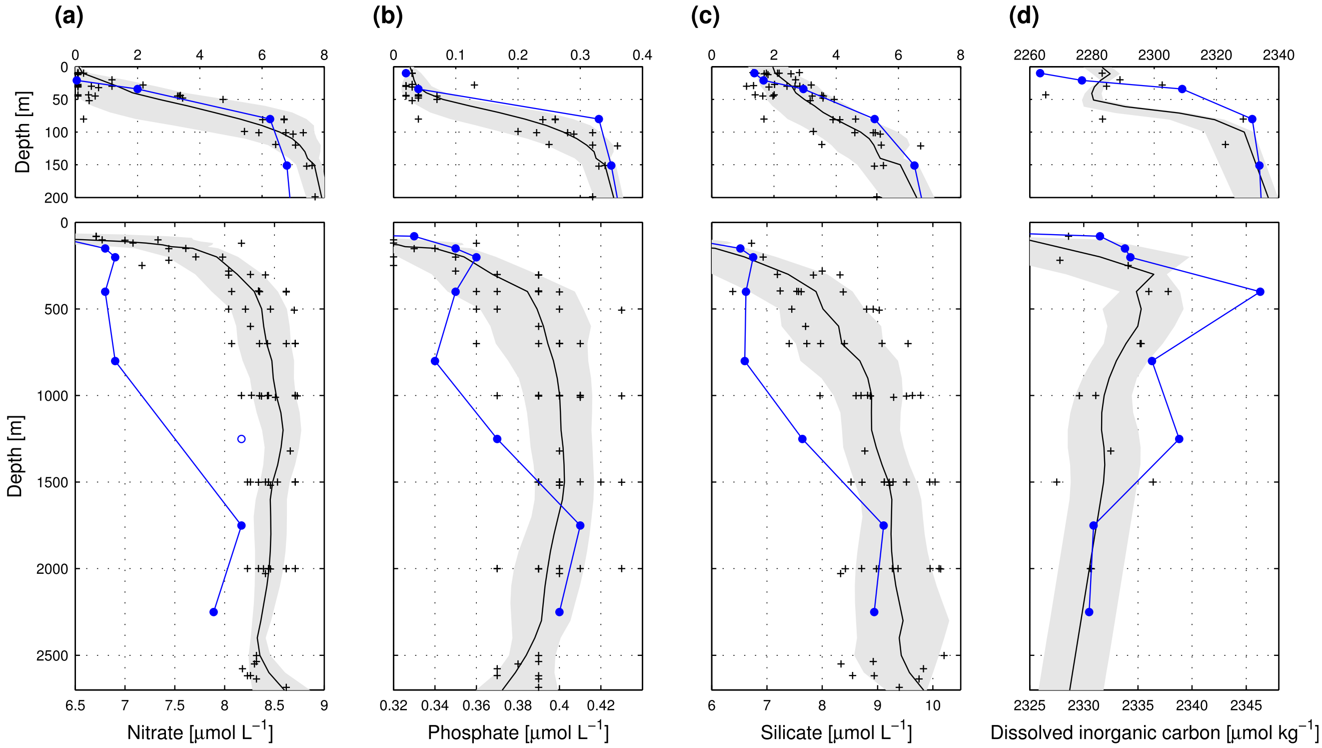

Figure 8. Concentrations of the three main nutrients and carbon measured during the MOOSE-GE 2013 cruise: (a) nitrate, (b) phosphate, (c) silicate ions, and (d) total carbon. The blue dots show the concentration within the SCV core, while black dots are from the other stations carried in the eastern part of the basin (i.e., longitude >6°E, see the corresponding stations in Figure 2a). The gray shaded area represents the standard deviation of the data.

taken along the same section a few days later on 19 and 20 February, while surface layers had already started to restratify after an intense wind event. However, CTD casts collected slightly southwest of the glider section revealed comparable deep mixed layers. This illustrates the high spatial and temporal variability of the convective area. The center of the Ligurian Sea convective zone could have been located slightly southwest of the Nice-Calvi glider section, as also suggested by satellite images [see *Houpert et al.*, 2016, Figure 8].

In terms of hydrographical characteristics, when the mixed layer was observed deeper than 600 m, it was characterized by a mean potential temperature close to 13.17°C and practical salinity close to 38.54. In a θ/S diagram, this water mass lies on the mixing line between LIW and WMDW and can be qualified as winter deep waters following *Bosse et al.* [2016]. The mixed layer was observed to be deeper than 600 m in the Gulf of Lions and characterized by colder and fresher characteristics of the newly formed WMDM (see Figure 1b).

3.2. SCV Characteristics

3.2.1. Hydrographical Description

During the MOOSE-GE 2013 cruise, a CTD cast carried out in the Ligurian Sea on 15 June revealed a particularly homogeneous layer of oxygenated waters between 300 and 1200 m depth ($\theta \sim 13.18$°C, $S_P \sim 38.54$, DO = 195–200 μmol kg^{-1}, see Figure 2b). Shortly after, a glider deployed along the repeated "Nice-Calvi" endurance line (mission MOOSE T00–26) crossed by chance the same water mass (see Figure 2c). From 600 to 900 m, potential temperature only increases by 0.0014° and salinity by 0.0015. The resulting vertical stratification is very weak: +0.0005 kg m^{-3} from 600 to 900 m and roughly constant potential density from 750 to 900 m (equivalent to $N \sim f$). This low stratified water is enclosed within an anticyclonic rotation. The deep isopycnals deformation is characteristics of Submesoscale Coherent Vortices (SCV) with a doming of isopycnals above its equilibrium depth and a deepening below it [*McWilliams*, 1985]. The presence of ventilated waters at such depths indicates a recent origin related to winter mixing. Figure 7 shows a salinity oxygen space the clear signature of the SCV between 300 and 1200 m. At the base of the core between 1200 and 1800 m, the oxygen content is lower than the surroundings and remarkably homogeneous. As described before, the convective area had about the same θ/S_P characteristics as the SCV around mid-February in the Ligurian Sea. This would indicate the SCV was formed about 4.5 month prior to its sampling during summer.

The SCV has a clear signature on heat, salt, and oxygen distribution over the water column. At intermediate depths where LIW are usually found, the SCV core has a lower temperature (-0.15°C) and salinity (–0.03). But, the more important signal is the clear increase of the temperature (up to $+0.2$°C) and salinity (up to $+$ 0.05) between 700 and 1800 m. In terms of oxygen, it has a positive anomaly at all depths reaching 17 μmol kg^{-1} at the LIW level characterized by low oxygen concentrations. In the deep layers below 1700 m, salinity is systematically smaller than the surroundings with salinities of 38.48. This value is typical of the WMDW observed prior to the intense production of saltier deep waters during winter 2013 [*Houpert et al*., 2016; *Testor et al.,* 2017]. The SCV would impact the whole water column down to the bottom, likely due to its important barotropic rotation able to trap old deep waters during its formation.

Interestingly, quite marked LIW are found in the rim of the eddy ($\theta \sim 13.45$°C and $S \sim 38.59$) compared to typical values found in the Ligurian Sea (see Figure 4). Figure 3a shows the potential temperature at 400 m in an eddy-centered frame where every observation has been rotated according to its orbital velocity and observation date. This horizontal view shows the heterogeneity of the LIW temperature at the rim of the eddy, unlike the very homogeneous core (see Figure 3b, left). Some profiles located between one and two radius reveal temperature reaching 13.61°C and salinity up to 38.63. Such values are only found along the continental slope off Corsica (see Figure 2c), the boundary circulation along Sardinia and Corsica being known as a major inflow of warm and salty LIW to the NW Mediterranean Sea [*Millot*, 1987; *Bosse et al*., 2015]. The SCV would have recently been interacting with this LIW vein without being affected, as the core remains very homogeneous while parts of the LIW vein have clearly been extracted and exported to the open-sea.

3.2.2. Dynamical Description

3.2.2.1. Cyclogeostrophic Velocities

They show a clear maximum $V^{max}=13.9\pm2.0$ cm s^{-1} at $R=6.2\pm0.2$ km from the center. The peak velocity is found at 700 m depth where the geostrophic shear (i.e., isopycnals slope) changes sign (see Figure 5a). Close to the surface, velocities are significantly smaller (about 4 cm s^{-1} at the surface, 7 cm s^{-1} at 100 m) supported by LADCP measurements. Baroclinic velocities account for about 20% of the total velocities, the rotation of this SCV appears to be mainly barotropic. This could be the reason why the SCV also has a signature in the deep waters below its oxygenated core. Ageostrophic cyclotrophic velocities reach 3.8 cm s^{-1} at a radial distance of 4.1 km smaller than the eddy radius. Ageostrophy is maximum at the origin and represents from about 10% at the surface up to $\sim$45% around 700 m (see Figure 5a, right). This confirms the important role of centrifugal effects in the balance of small-scale SCVs.

3.2.2.2. Rossby Number

When normalized by the planetary vorticity *f*, the vorticity $\zeta(r,z)$ represents a local Rossby number $Ro_l(r,z)$ that quantifies the nonlinearity of the flow. Due to its small radius and intense orbital velocities, the relative vorticity of the SCV reaches pretty high values of $-0.80f$ at the eddy core, close to –*f* the limit set by inertial instability for barotropic vortices [*Kloosterziel et al*., 2007]. This value is very similar to $-0.85f$ reported by *Prater and Sanford* [1994] in a small Meddy in the Atlantic. Flow with large Rossby number close to unity is qualified as submesoscale flows, as they are not completely in geostrophic balance (see a recent review by *McWilliams* [2016] for more details). The Rossby number of the SCV, estimated at the velocity maximum as $Ro \equiv 2V^{max}/Rf$, ends up to be -0.45 ± 0.08, comparable to previous estimates associated with postconvective SCVs in the NW Mediterranean Sea [*Testor and Gascard*, 2006; *Bosse et al*., 2016]. *McWilliams* [1985] suggested that SCVs can survive interactions with external flows characterized by weaker horizontal shear. Here the high vorticity of the SCV could make it survive interactions with boundary flows mostly in geostrophic balance (horizontal shear of about $0.1f$ or smaller). This also provides a rational explanation for the presence of the warm and salty LIW observed at the rim of the eddy that could result from its interaction with the LIW flow off Corsica (see Figures 3 and 4).

3.2.2.3. Burger Number

The horizontal scale of oceanic eddies is controlled by the internal deformation radius: $R_d \equiv NH/f$ depending on *H* its vertical extension and *N* the water column stratification ($N^2 \equiv -g\partial_z\sigma/\rho_0$). The stratification generally decreases with depth: here $N \leq 5f$ below 500 m (see Figure 5c). This explains why subsurface eddies have a small radius compared to surface mesoscale eddies. The Burger number further quantifies the ratio of the deformation radius to the eddy radius: $Bu \equiv [NH/fR]^2 = [R_d/R]^2$. To compute the Burger number of the SCV, $H = 1600$ m is defined from the vertical extension of its geopotential anomaly at the center (i.e., larger than 20% of its maximum value at 700 m) and $N = (4.0 \pm 0.4)f$ is the mean background stratification between 600 and 800 m. This yields a Burger number of 1.14 ± 0.22, close to unity. In a low stratified ocean, eddies have thus an unusual high aspect ratio ($R/H \sim N/f \in [1:10]$). This is a particular feature shared by many SCVs observed around the world's oceans [*D'Asaro*, 1988; *Timmermans et al*., 2008; *Bower et al*., 2013; *Pelland et al*., 2013; *Bosse et al*., 2015], which can be theoretically explained in an idealized case [*Carpenter and Timmermans*, 2012].

3.2.2.4. Effect on Stratification and Potential Vorticity

The vertical stratification is significantly weakened inside the SCV almost to a factor of 2 with a mean value $2.4f$ at ~700 m (see Figure 5c). Although there are few deep observations, the stratification increases close to the bottom, as observed at the base of deep anticyclonic SCVs [*Bosse et al*., 2016]. Combined with the strong negative vorticity, the PV is notably reduced up to a factor of 20 inside the core at the depth of the vorticity maximum and minimum of stratification. The PV reaches values as low as 10^{-13} m s^{-1}, which is 1 order of magnitude smaller than that of LIW SCVs formed by topographic interaction in the NW Mediterranean Sea [*Bosse et al*., 2015]. The PV conservation between an initial resting water parcel and the final rotating state enables to compute the initial stratification of the resting fluid parcel: $N_{ini} = N_{scv}\sqrt{1+Ro_l(0,700)} = 1.1f$. Such a low value confirms that convective processes might be at the origin of the SCV.

3.3. Dynamical Barriers

By resolving the diffusion equation, a lateral isopycnic diffusion coefficient could be estimated for each tracer at different depths (see Figure 6). Around to the velocity maximum between 550 and 800 m, the lateral gradient of temperature and salinity is too weak and no estimation is possible. Where it can be estimated, K_ρ is 0.22 ± 0.04 m^2 s^{-1}. The tracer distribution reaches background values at the radial distance of about $\sqrt{2}r_0$ (=8.9 km), where the relative vorticity becomes positive. This is also where the strain rate is maximum (see Figure 5b). The dynamical barriers of the SCV seem to start there and extend to the eddy center.

As explained in section 2.5, dissolved oxygen is the only tracer that provides K_ρ estimates near the equilibrium depth of the SCV, where the horizontal vertical processes might be the smallest. There are consistent values among the different tracers, except below the core, where oxygen diffusivity seems to slightly diverge. This could be the effect of the unknown biological processes acting on the oxygen budget of the SCV. Indeed, *Budéus et al*. [2004] showed a stimulation of the bacterial activity in deep convective SCVs observed in the Greenland Sea. However, this idea remains hard to verify here without dedicated measurements. Furthermore, the base of the SCV's core is a region of stronger stratification and where trapped near-inertial waves could enhance turbulence levels [*Kunze et al*., 1995; *Sheen et al*., 2015]. Diapycnal mixing could then increase there, pushing to the limit our simple 1-D diffusion model. Again, with no turbulence measurements, we can unfortunately not test this idea. Overall, all estimates agree on the order of magnitude of the diffusion coefficient of 0.2 m^2 s^{-1}.

Okubo [1971] reviewed estimates of the horizontal eddy diffusivity coefficient associated with oceanic turbulence and its scale dependency ranging 1–100 m^2 s^{-1} for scales of 1–100 km (see also a nice and more recent review in introduction of *Nencioli et al*. [2013]). Here we quantified the integral effect of unresolved small-sale processes on the erosion of the SCV's core. This has been previously done for Meddies in the Atlantic Ocean: *Hebert et al*. [1990] found a lateral eddy coefficient of 5 m^2 s^{-1} associated with the decay of a 20 km radius Meddy and *McWilliams* [1985] 10 m^2 s^{-1} for a typical 50 km radius Meddy. If Meddies and postconvective SCVs have a comparable lifetime T of a few years, the smaller radius L of SCVs would tend to reduce their associated diffusion coefficient ($\propto L^2\,T^{-1}$). The physics of the dissipation of Meddies and postconvective SCVs is likely to involve different processes. While the rim of Meddies is a place of intense layering [*Meunier et al*., 2015] and their core is known to be subjected to double diffusive convection and salt-fingering [*Armi et al*., 1989], the SCV studied here does not exhibit the typical features associated with those processes (horizontal interleaving or vertical staircases in temperature and salinity).

As stated before, *McWilliams* [1985] highlighted the link between the SCV vorticity and its ability to overcome interactions with external flows. Here the extreme negative vorticity ($-0.8f$) sets important dynamical barriers within the core that drastically inhibit lateral exchanges. The background flow is typically characterized by velocities around 10 cm s^{-1} at 500 m depth and horizontal scales of about 10 km, leading to horizontal shear order of $0.1f$. Recently, *Damien et al.* [2017] managed to simulate postconvective SCVs of 5 km radius in a realistic high-resolution regional simulation. The SCVs similarly show a slow diffusion of their core properties with an diffusion coefficient of 0.6 m^2 s^{-1} in coherence with our estimates. They could survive many interactions with external flows before being finally dissipated by the convective event occurring the following winter.

3.4. Biogeochemical and Biological Impacts

3.4.1. Impact on Nutrients Concentration

The SCV has an important impact on the nutrients distribution (see Figures 8a–8c). Close to the surface, all nutriclines seem to be shallower by 20–50 m compared to the background environment leading to an enhancement of the nutrient availability at the base of the euphotic layer. Within the SCV core between 300 m and about 1500 m depth, the three main nutrients (nitrate, phosphate, and silicate) are significantly depleted with respective concentrations around 700 m of 6.9, 0.34, and 6.6 μmol L^{-1}. This is a decrease of 18, 13, and 18% compared to background concentrations. As for other tracers, nutrients remain isolated from the surrounding environment because of the very limited lateral exchanges.

The formation process of the SCV can provide an explanation for these low values. Indeed, it results from the mixing of nutrients-poor surface waters with richer waters. Schematically, a 100 m thick surface layer with no nutrients being mixed with 700 m of nutrient-rich waters below would result in a nutrient concentration reduced by about 13%. Following this argument, among the other type of postconvective SCVs described in *Bosse et al*. [2016], anticyclones with a deep core below 1000 m and cyclones of newly formed deep waters would certainly have a less marked imprint on the nutrients, whereas shallower winter intermediate water SCVs would be even more nutrients depleted.

3.4.2. Impact on Phytoplankton

The radial distribution of chlorophyll-a measured by the glider is shown in Figure 9a. Both $[Chl_a]$ at the deep chlorophyll maximum (DCM) and integrated over the top 200 m reveal much higher concentrations inside the eddy with, respectively, 1.7 mg m^{-3} (+113%) and 29 mg m^{-2} (+38%) (Figures 9b and 9c). The eddy dynamics seems thus to favor phytoplankton growth, much likely as a result of the isopycnals doming characteristic of cyclonic and “Mode Water” anticyclones [*McGillicuddy et al*., 2007; *Nencioli et al*., 2008]. The isopycnals doming is quite marked at about 100 m deep, while it is dumped closer to the surface due to summer stratification. This can explain why nutriclines are displaced of about 20–50 m increasing the nutrients availability, whereas the DCM only moves by less than 10 m (Figure 9d).

Regarding the phytoplankton size group, HPLC measurements show a clear predominance of nanophytoplankton inside the eddy with a concentration of 0.86 mg m^{-3}, about twice the median value of 0.44 mg m^{-3} observed in the Ligurian Sea (see Figure 9e). This is one of the most abundant station for nanophytoplankton, which represents almost 80% of the total chlorophyll-a. Note that the glider fluorometer calibrated with satellite images is in good agreement with the total chlorophyll-a concentration of 1.1 mg m^{-3} measured by HPLC.

4. Discussion

4.1. Fate and Decline of Postconvective SCVs

Deep SCVs are among the most coherent circulation features in the ocean and represent local oddities for the diffusion of tracers. For the diffusive cylinder, the tracer concentration will reach half of its initial value after $L^2/0.20K_\rho$. Given the diffusion coefficient estimated here, it yields a typical lifetime of 28 months. The SCVs here observed 4.5 months after its formation can be considered as still being in its early stage of life. This is new evidence of the extended lifetime of SCVs already observed [*Testor and Gascard*, 2003; *Budéus et al*., 2004; *Testor and Gascard*, 2006; *Bosse et al*., 2016].

For long, it has been considered that lateral intrusions driven by double-diffusion are causing the decay of Meddies. However, new theories on the origin of those intrusions were recently made implying flow

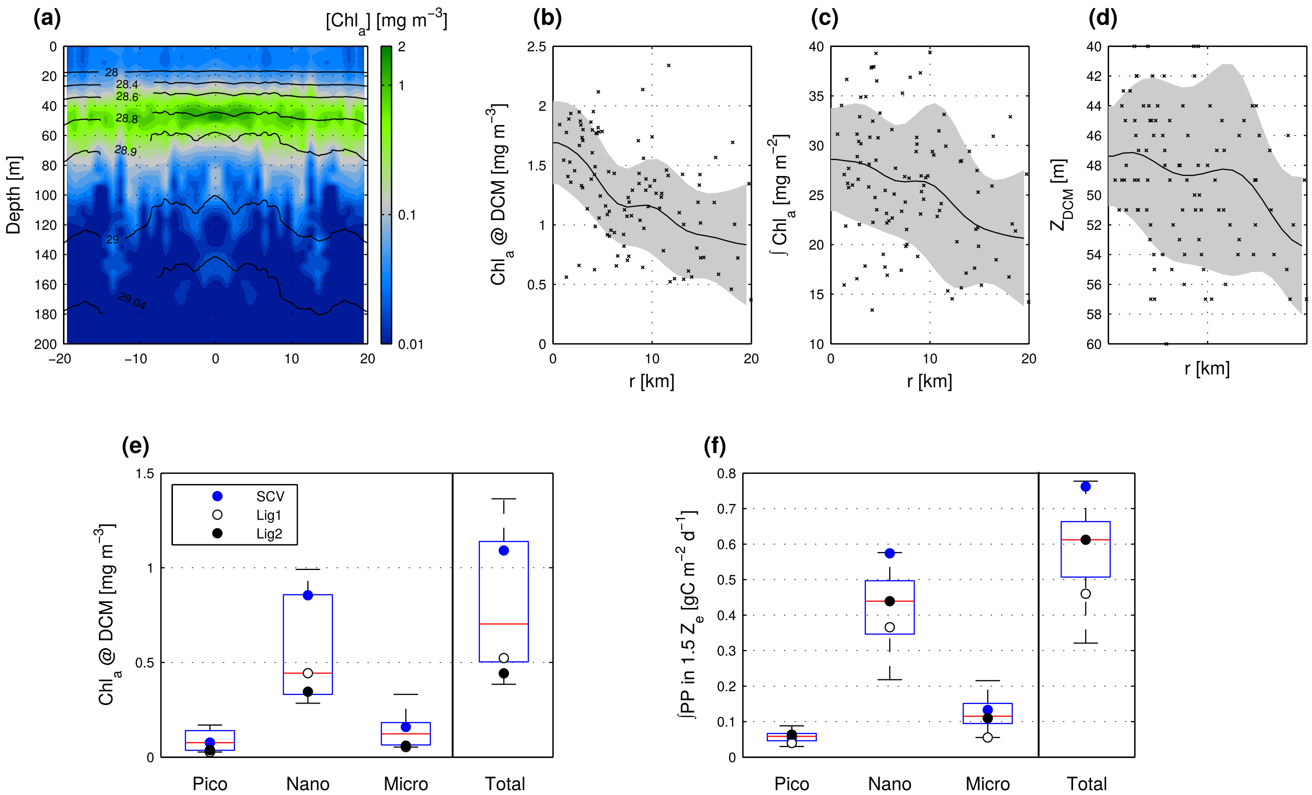

Figure 9. (a) Bin-averaged section across the eddy of the chlorophyll-a concentration measured by the glider. Black contours show the isopycnals. Note that a radial symmetry has been applied for aesthetic and clarity purposes. Radial distribution of (b) the chlorophyll-a concentration measured at the deep chlorophyll maximum; (c) the integrated chlorophyll-a concentration over the top 200 m; and (d) the depth of this deep chlorophyll maximum. (e) Chlorophyll-a concentration of three phytoplankton size classes. (f) Primary production associated with each size group. The box plots were constructed using all measurements carried out during the MOOSE-GE 2013 cruise in the eastern part of the basin (i.e., longitude $>6^{\circ}$E, see the corresponding stations in Figure 2a). The red mark is the median, the box limits the 25th and 75th percentile and the whiskers show the extension of the data set. The particular SCV core station is highlighted in blue, as well as the two closest HPLC stations carried out in the Ligurian Sea (Lig1 and Lig2).

instability and stirring processes [*Hua et al.*, 2013; *Meunier et al.*, 2015]. Here it is hard to see any intrusion at the rim of the SCV, the gradients separating the SCV and the surroundings being pretty sharp for each eddy crossing by the glider (see Figure 2c). Anticyclonic eddies can also trap downward propagating near-inertial waves, as it has already been observed [*Joyce et al.*, 2009; *Cuypers et al.*, 2012; *Sheen et al.*, 2015; *Karstensen et al.*, 2017]. The energy dissipation of those waves and their influence on the decay of small-scale postconvective SCVs would need to be assessed in future studies with help of complementary turbulence measurements and numerical models.

4.2. Deep Mixing Preconditioning

As SCVs can live for an extended period of time and are very resistant to interactions, they can easily survive until the following winter. Vertical mixing is actually a primary generation mechanism of SCVs, but plays also likely an important role in their dissipation. Due to the deformation of isopycnal layers associated with them, they also have an influence on the deepening of the mixed layer [*Legg et al.*, 1998; *Lherminier et al.*, 1999; *Bosse et al.*, 2015, 2016]. For an anticyclonic SCV, once the vertical mixing reaches the top of its weakly stratified core, it then requires a lot less buoyancy loss to mix it down to the base of the core.

The heat and salt content anomalies integrated between the center and one eddy radius represent, respectively, $+4.0\times10^{9}$ kg of salt and $+4.7\times10^{16}$ J. These values are comparable to what was found for LIW SCVs by *Bosse et al.* [2015]. This suggests that postconvective SCVs of winter deep waters can have an equally important role in the vertical and horizontal heat/salt transport across the NW Mediterranean. The large amount of heat and salt they transport can eventually be redistributed

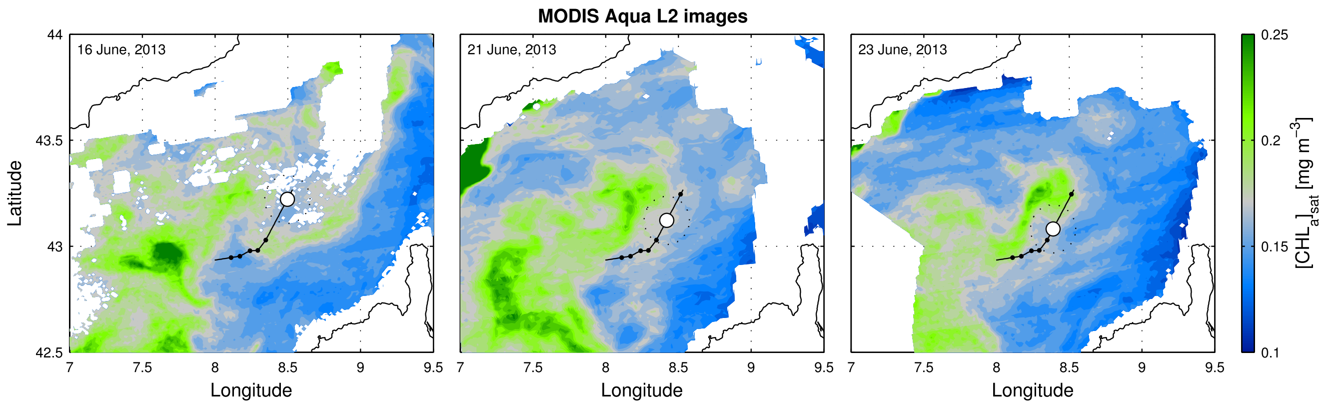

Figure 10. Remotely sensed chlorophyll-a concentration at the ocean surface measured by MODIS Aqua scatterometer in June 2013 in the Ligurian Sea. The black dots are the eddy center deduced by in situ observations. The white dot is the interpolated eddy center position at the moment the images were taken. A circle of is 12.6 km radius ($=2r_0$) is drawn to show the eddy outer extension. Note that these are the only good images found from 13 June to 7 July.

within the mixed layer, thus impacting the heat/salt budget of the deep waters, as discussed by *Bosse et al.* [2015] for LIW SCVs.

4.3. Surface Signature of a Subsurface SCV

The detection of subsurface eddies from space is an active research topic (see *Klemas and Yan* [2014] for a review). However, in weakly stratified oceans like the Mediterranean Sea characterized by a small deformation radius, gridded altimetry products have a too large decorrelation scale compared to the observed oceanic variability associated with SCVs and standalone along-track measurements that could tentatively resolve them are hard to interpret. In this context, ocean color images can be very useful, as they provide insights at very high resolution (1 km) into the surface dynamics at the only condition that the sky remains cloud-free. Sea surface temperature measured by satellite at high resolution has also been examined. Figure 4a indeed suggests that surface waters are 0.1–0.2°C colder inside the eddy. However, the summertime heating of the superficial layers very likely prevents such a signal to be captured.

Figure 10 shows the evolution of the surface chlorophyll-a concentration seen by satellite. It reveals a clear clockwise swirling of a chlorophyll patch around the outer edge of the deep SCV. Despite lower velocities of about 5 cm s^{-1}, the SCV seems, however, to act on the surface dynamics (see Figure 5a). Like at great depths, dynamical barriers similarly prevent lateral exchanges between the eddy core and the surroundings. Generally, the surface chlorophyll signal associated with subsurface postconvective SCVs would then be sensitive to the context of its surrounding environment, unlike its subsurface signature characterized by an enhanced deep chlorophyll maximum.

4.4. Primary Production and Carbon Sequestration

The primary production is estimated from HPLC measurements by applying a bio-optical model [*Morel*, 1991]. It shows an important influence of the SCV compared to other stations carried out in the Ligurian Sea (see Figure 9f). The total primary production reaches 0.76 gC m^{-2} d^{-1} about 25% more than the average value in the Ligurian Sea (0.6 gC m^{-2} d^{-1}). The contribution of the different phytoplankton size groups to this elevated primary production again reveals the importance of nanophytoplankton. This can have further implication for the carbon sequestration, as higher productivity also means enhanced export of particulate organic carbon to great depths where it can be remineralized under the action of bacteria. Higher carbon export within mesoscale eddies was already reported in Mediterranean Sea by *Moutin and Prieur* [2012]. *Waite et al.* [2016] recently described an important mechanism that concentrates particulate export within mesoscale eddies. The remineralization would imply a gradual increase in the nutrients concentration. The SCV's core however remained nutrients-depleted even after more than 4 months of remineralization.

Dissolved inorganic carbon measurements also reveal a higher concentration within the SCV of about 5–10 μmol kg^{-1}. As discussed before, this could result from the higher productivity associated with it. Another explanation could be the trapping at depth of organic carbon during wintertime, while the SCV is formed. Indeed, Figure 1c shows a clear signal of chlorophyll-a below the euphotic layer within the mixed layer and down to 1000 m. Phytoplankton cells initially present in the surface layer are then diluted over the mixed layer during active mixing characterized by intense vertical water displacements of $\pm$5–15 cm s^{-1} [*Schott and Leaman*, 1991; *Marshall and Schott*, 1999; *Margirier et al.*, 2017]. This allows within a few hours the overturning of phytoplankton between the euphotic layer and depths of about 1000 m. During the generation of postconvective SCV, vertical motions cease and phytoplankton would get trapped within the deep core before being converted into inorganic carbon.

5. Summary and Conclusion

This study described the dynamical and biogeochemical characteristics of a Submesoscale Coherent Vortex (SCV) formed by deep convection in the Ligurian Sea (NW Mediterranean Sea). It is based on in situ observations collected in late June 2013 during a research cruise (shipborne CTD measurements and water samples analysis) combined with data from an autonomous glider equipped with optode and bio-optical sensors. It was very fortunate that the glider crossed the eddy a few days after the ship, but the opportunity was taken to intensively sample the eddy with the glider.

Its core is made of nearly homogeneous water between 300 and 1200 m depth with $\theta \simeq 13.18°$C, $S_P \simeq 38.54$, and DO $\simeq$ 200 μmol kg^{-1}. The high dissolved oxygen concentration of the SCV indicates an origin during the previous wintertime convective episode about 4.5 month prior to its sampling during summer. The presence of very warm and salty Levantine intermediate waters around it suggests it has been interacting with the boundary circulation flowing along the continental slope along Sardinia and Corsica.

The SCV has an intense anticyclonic rotation with depth-average currents measured by the glider up to 15 cm s^{-1}. Those currents were used to detect the eddy center and reconstruct the fine-scale eddy dynamics. The equilibrium depth of the SCV is around 700 m, where cyclogeostrophic peak velocities of 13.9 cm s^{-1} are estimated at a distance of 6.2 km from the center. The force balance of the eddy is found to be strongly nonlinear with a Rossby number at the velocity maximum of -0.45. The shear at the origin is even higher and reaches $-0.8f$. This suggests a great ability of the SCV to overcome the interaction with external flows. The Burger number of the SCV is close to unity indicating a high aspect ratio of this circulation feature. The vertical stratification N is reduced within the core with a mean core stratification of about $2.4f$. Due to this low value and to the high anticyclonic vorticity, the potential vorticity of the SCV reaches values as low as 10^{-13} m^{-1} s^{-1} testifying to the strong mixing occurring during its generation.

The extensive sampling of the eddy core and the knowledge of the age of the eddy enable to estimate a lateral isopycnic coefficient by solving the cylindrical diffusion equation. It yields a diffusive coefficient of 0.22 m^2 s^{-1}. The diffusive half-life of the eddy is thus of about 2.5 years. So, even after 4.5 months of existence, the SCV can still be considered as being in its early stage of life. Important dynamical barriers drastically reduce lateral exchanges between the core of the SCV and the surroundings thus enabling it to keep the characteristics of its origin (i.e., ventilated waters with almost constant temperature and salinity). Furthermore, it has the ability to easily survive until the following winter. As interactions with other flows and diffusive processes have little impact on the SCV, winter vertical mixing is likely to be an important mechanism for the destruction of such very coherent SCVs. In the future, the utilization of turbulence sensors mounted on gliders could unveil the mysteries about the SCVs fate and in particular their interaction with internal waves.

In terms of biogeochemical properties, the SCV core is nutrient-depleted with concentrations in nitrate, phosphate, and silicate on average -15% lower than what is found in the surroundings at about 700 m. Nutriclines are shifted toward the surface by about 20–50 m, enhancing the nutrients availability for phytoplankton growth. Consistently, the glider fluorometer and HPLC measurements reveal higher chlorophyll-a concentrations of the deep chlorophyll maximum within the eddy (1.7 mg m^{-3}, +90%). Furthermore, pigments concentrations show a clear predominance of nanophytoplankton compared to outside. This demonstrates that even deep SCVs have a significant influence on the nutrients distribution and the phytoplankton community. A bio-optical model was also used to characterize the primary production. It was found to be significantly enhanced inside the SCV leading potentially to a higher carbon sequestration.

This study gives the first conjoint physic-biogeochemical description of a postconvective SCV in the NW Mediterranean Sea. Our findings suggest they locally have a great imprint on both physical and biogeochemical cycles. However, their basin-scale impact in particular for the nutrients budget or the phytoplankton distribution still need to be assessed. This is an important issue for coupled regional climate model that do not resolve those processes, but still aim at characterizing the evolution of the marine ecosystem in the context of climate change.

Appendix A: The Heat Equation in Cylindrical Coordinate

Let us consider the evolution of a tracer T whose concentration is initially constant $T=T_0$ and confined within a long cylinder of radius R. In this case, the heat equation goes by in its cylindrical form,

$$\frac{\partial T}{\partial t}=K\frac{1}{r}\frac{\partial}{\partial r}\left(r\frac{\partial T}{\partial r}\right). \tag{A1}$$

The desired solution of this equation owes to verify (1) $\partial_r T=0$ at $r=0$ as imposed by the cylindrical geometry and (2) $T=T_\infty$ at $r=L$ as the background domain is supposed to be infinite and thus have a constant tracer concentration.

According to the separation of variables method, we can seek a solution of the form: $T(r,t)=T_\infty+\alpha(r)\beta(t)$. Substituting this into the heat equation yields,

$$\frac{1}{r\alpha}\frac{d}{dr}\left(r\frac{d\alpha}{dr}\right)=\frac{1}{K}\frac{1}{\beta}\frac{d\beta}{dt}. \tag{A2}$$

Each side of the equation being a function of an independent variable (r and t), it has thus to be constant. Furthermore, this constant must be negative to prevent β from exponentially diverging in time. Let us call it $-\lambda^2$, we then have,

$$r^2\frac{d^2\alpha}{dr^2}+r\frac{d\alpha}{dr}+r^2\lambda^2=0 \ \text{ and } \ \frac{d\beta}{dt}+K\lambda^2\beta=0. \tag{A3}$$

The general solution for β is simply: $\beta(t)=\beta_0 e^{-\lambda^2 Dt}$ where β_0 is a constant.

The equation on α is a special case of Bessel's equation, whose only physically meaningful solution has the form: $\alpha(r)=\alpha_0 J_0(\lambda r)$, where α_0 is another constant and J_0 is the Bessel function of first kind of order zero.

Since $T(r=L,t)=T_\infty$, this requires $J_0(\lambda L)=0$. Knowing the zeros of the Bessel function J_0, one can thus define λ_n the eigenvalues of the problem and the particular solutions for the problem: $T_n(r,t)=T_\infty+A_nJ_0(\lambda_n r)$ $e^{-\lambda_n^2 Dt}$ with $A_n=\alpha_0^n\beta_0$. The general solution then writes,

$$T(r,t)=T_\infty+\sum_{n=1}^{\infty}A_nJ_0(\lambda_n r)e^{-\lambda_n^2 Kt}. \tag{A4}$$

To infer the coefficients A_n, one can project the initial condition $(T(r,t=0)-T_\infty=T_0-T_\infty)$ onto a particular eigenfunction $J_0(\lambda_m r)$ and use the orthogonality of each eigenfunction $\left(\int_{[0,L]} rJ_0(\lambda_m r)J_0(\lambda_n r)dr=0 \text{ if } n\neq m, \ =1\text{otherwise}\right)$,

$$\int_0^L rJ_0(\lambda_m r)(T_0-T_\infty)dr=\sum_{n=1}^{\infty}\int_0^L rA_nJ_0(\lambda_m r)J_0(\lambda_n r)dr=A_m\int_0^L rJ_0(\lambda_m r)^2dr. \tag{A5}$$

Then knowing that $\int_{[0,L]} rJ_0(\lambda_m r)dr=LJ_1(\lambda_m L)/\lambda_m$ and $\int_{[0,L]} rJ_0^2(\lambda_m r)dr=L^2[J_0^2(\lambda_m L)+J_1^2(\lambda_m L)]/2=L^2J_1^2(\lambda_m L)/2$, one can explicit the different coefficient A_m and write the final solution of our problem,

$$T(r,t)=T_\infty+\frac{2(T_0-T_\infty)}{L}\sum_{n=1}^{\infty}\frac{J_0(\lambda_n r)}{\lambda_n J_1(\lambda_n L)}e^{-\lambda_n^2 Kt}. \tag{A6}$$

Acknowledgments
The hydrographical data were collected and made freely available by the Coriolis project and programs that contribute to it (http://www.coriolis.eu.org). The cruise data are provided in the reference section along with the associated doi. Vincent Tailliandier is thanked for the calibration of shipborne CTD and providing feedback on the manuscript. We would like to acknowledge the staff of the French National Pool of Gliders of DT-INSU (CNRS/Ifremer) for the sustained gliders deployments carried out in the framework of MOOSE, as well as the intensive deployments during this 2012–2013 DEWEX experiment. Captains and crew of R/V *Le Tethys II* (CNRS/INSU) and *Le Suroit* (Ifremer) as well as all scientists, engineers, and technicians who participated to the MOOSE-GE and DEWEX different cruises and autonomous platforms deployments are also warmly thanked. Support was provided by the French the French "Chantier Méditrranée" MISTRALS program (HyMeX and MERMeX components) and the French MOOSE long-term observatory (SOERE/AllEnvi-SNO/INSU), as well as by the EU projects FP7 GROOM (grant 284321), FP7 PERSEUS (grant 287600), and FP7 JERICO (grant 262584) and the COST Action ES0904 "EGO" (Everyone's Gliding Observatories). A. Bosse was funded by a French government scholarship.

References

Aminot, A., and R. Kérouel (2007), Dosage Automatique des Nutriments Dans les Eaux Marines, 188 pp., Ifremer, France.
Armi, L., D. Hebert, N. Oakey, J. F. Price, P. L. Richardson, H. T. Rossby, and B. Ruddick (1989), Two years in the life of a Mediterranean salt lens, *J. Phys. Oceanogr.*, *19*, 354–370.
Béthoux, J.-P., B. Gentili, J. Raunet, and D. Tailliez (1990), Warming trend in the western Mediterranean deep water, *Nature*, *347*, 660–662.
Bosse, A. (2015), Circulation générale et couplage physique-biogéochimie à (sous-)mésoéchelle en Méditerranée Nord-occidentale à partir de données in situ, PhD thesis, Univ. Pierre et Marie Curie, Paris.
Bosse, A., P. Testor, L. Mortier, L. Prieur, V. Taillandier, F. D'Ortenzio, and L. Coppola (2015), Spreading of Levantine Intermediate Waters by submesoscale coherent vortices in the northwestern Mediterranean Sea as observed with gliders, *J. Geophys. Res. Oceans*, *120*, 1599–1622, doi:10.1002/2014JC010263.
Bosse, A., et al. (2016), Scales and dynamics of submesoscale coherent vortices formed by deep convection in the northwestern Mediterranean Sea, *J. Geophys. Res. Oceans*, *121*, 7716–7742, doi:10.1002/2016JC012144.
Bouffard, J., A. Pascual, S. Ruiz, Y. Faugère, and J. Tintoré (2010), Coastal and mesoscale dynamics characterization using altimetry and gliders: A case study in the Balearic Sea, *J. Geophys. Res.*, *115*, C10029, doi:10.1029/2009JC006087.
Bouffard, J., L. Renault, S. Ruiz, A. Pascual, C. Dufau, and J. Tintoré (2012), Sub-surface small-scale eddy dynamics from multi-sensor observations and modeling, *Prog. Oceanogr.*, *106*, 62–79.
Bower, A. S., R. M. Hendry, D. E. Amrhein, and J. M. Lilly (2013), Direct observations of formation and propagation of subpolar eddies into the subtropical North Atlantic, *Deep Sea Res., Part II*, *85*, 15–41.
Bretherton, F. P., R. E. Davis, and C. B. Fandry (1976), A technique for objective analysis and design of oceanographic experiments applied to MODE-73, *Deep Sea Res. Oceanogr. Abstr.*, *23*, 559–582.
Budéus, G., B. Cisewski, S. Ronski, D. Dietrich, and M. Weitere (2004), Structure and effects of a long lived vortex in the Greenland Sea, *Geophys. Res. Lett.*, *31*, L05304, doi:10.1029/2003GL017983.
Carpenter, J. R., and M.-L. Timmermans (2012), Deep mesoscale eddies in the Canada Basin, Arctic Ocean, *Geophys. Res. Lett.*, *39*, L20602, doi:10.1029/2012GL053025.
Ciani, D., X. Carton, I. Bashmachnikov, B. Chapron, and X. Perrot (2015), Influence of deep vortices on the ocean surface, *Interdiscip. J. Discontin. Nonlinearity Complex.*, *4*, 281–311.
Claustre, H. (1994), The trophic status of various oceanic provinces as revealed by phytoplankton pigment signatures, *Limnol. Oceanogr.*, *39*, 1206–1210.
Cotroneo, Y., G. Aulicino, S. Ruiz, A. Pascual, G. Budillon, G. Fusco, and J. Tintoré (2015), Glider and satellite high resolution monitoring of a mesoscale eddy in the Algerian basin: Effects on the mixed layer depth and biochemistry, *J. Mar. Syst.*, *162*, 73–88.
Cuypers, Y., P. Bouruet-Aubertot, C. Marec, and J.-L. Fuda (2012), Characterization of turbulence from a fine-scale parameterization and microstructure measurements in the Mediterranean Sea during the BOUM experiment, *Biogeosciences*, *9*, 3131–3149.
D'Asaro, E. (1988), Observations of small eddies in the Beaufort Sea, *J. Geophys. Res.*, *93*, 6669–6684.
Damien, P., A. Bosse, P. Testor, P. Marsaleix, and C. Estournel (2017), Modeling postconvective submesoscale coherent vortices in the northwestern Mediterranean Sea, *J. Geophys. Res. Oceans*, doi:10.1002/2016JC012114, in press.
DOE (1994), Handbook of Methods for the Analysis of the Various Parameters of the Carbon Dioxide System in Sea Water, version 2, ORNL/CDIAC-74, edited by A. G. Dickson and C. Goyet. [Available at http://cdiac.ornl.gov/DOE_94.pdf.]
Durrieu de Madron, X., et al. (2011), Marine ecosystems' responses to climatic and anthropogenic forcings in the Mediterranean, *Prog. Oceanogr.*, *91*, 97–166.
Durrieu de Madron, X., et al. (2017), Deep sediment resuspension and thick nepheloid layer generation by open-ocean convection, *J. Geophys. Res. Oceans*, *122*, 2291–2318, doi:10.1002/2016JC012062.
Elliott, B. A., and T. B. Sanford (1986), The subthermocline Lens D1. Part II: Kinematics and dynamics, *J. Phys. Oceanogr.*, *16*, 549–561.
Ertel, H. (1942), Ein neuer hydrodynamischer wirbelsatz, *Meteorol. Z.*, *59*, 277–281.
Estournel, C., et al. (2016), HyMeX-SOP2: The field campaign dedicated to dense water formation in the north-western Mediterranean, *Oceanography*, *29*(4), 196–206.
Fan, X., U. Send, P. Testor, J. Karstensen, P. Lherminier, and G. Drive (2013), Observations of Irminger Sea anticyclonic eddies, *J. Phys. Oceanogr.*, *43*, 805–823.
Frajka-Williams, E., P. B. Rhines, and C. C. Eriksen (2009), Physical controls and mesoscale variability in the Labrador Sea spring phytoplankton bloom observed by Seaglider, *Deep Sea Res., Part I*, *56*, 2144–2161.
Garau, B., S. Ruiz, W. G. Zhang, A. Pascual, E. E. Heslop, J. Kerfoot, and J. Tintoré (2011), Thermal lag correction on Slocum CTD glider data, *J. Atmos. Oceanic Technol.*, *28*, 1065–1071.
Gascard, J.-C. (1978), Mediterranean deep water formation baroclinic instability and oceanic eddies, *Oceanol. Acta*, *1*, 315–330.
Gascard, J.-C., A. J. Watson, M.-J. Messias, K. A. Olsson, T. Johannessen, and K. Simonsen (2002), Long-lived vortices as a mode of deep ventilation in the Greenland Sea, *Nature*, *416*, 525–527.
Gasparini, G. P., A. Ortona, G. Budillon, M. Astraldi, and E. Sansone (2005), The effect of the eastern Mediterranean transient on the hydrographic characteristics in the Strait of Sicily and in the Tyrrhenian Sea, *Deep Sea Res., Part I*, *52*, 915–935.
Hebert, D., N. Oakey, and B. Ruddick (1990), Evolution of a Mediterranean salt lens: Scalar properties, *J. Phys. Oceanogr.*, *20*, 1468–1483.
Houpert, L., et al. (2016), Observations of open-ocean deep convection in the northwestern Mediterranean sea: Seasonal and interannual variability of mixing and deep water masses for the 2007–2013 period, *J. Geophys. Res. Oceans*, *121*, 8139–8171, doi:10.1002/2016JC011857.
Hua, B. L., C. Ménesguen, S. Le Gentil, R. Schopp, B. Marsset, and H. Aiki (2013), Layering and turbulence surrounding an anticyclonic oceanic vortex: In situ observations and quasi-geostrophic numerical simulations, *J. Fluid Mech.*, *731*, 418–442.
Janzen, C., D. Murphy, and N. Larson (2007), Getting more mileage out of dissolved oxygen sensors in long-term moored applications, in OCEANS 2007, pp. 1–5, IEEE, doi:10.1109/OCEANS.2007.4449398.
Jones, H., and J. Marshall (1997), Restratification after deep convection, *J. Phys. Oceanogr.*, *27*, 2276–2287.

Joyce, T. M., L. N. Thomas, and F. Bahr (2009), Wintertime observations of subtropical mode water formation within the Gulf Stream, *Geophys. Res. Lett.*, *36*, L02607, doi:10.1029/2008GL035918.

Juza, M., L. Renault, S. Ruiz, and J. Tintoré (2013), Origin and pathways of winter intermediate water in the northwestern Mediterranean Sea using, *J. Geophys. Res. Oceans*, *118*, 6621–6633, doi:10.1002/2013JC009231.

Karstensen, J., et al. (2017), Upwelling and isolation in oxygen-depleted anticyclonic modewater eddies and implications for nitrate cycling, *Biogeosciences*, *14*, 2167–2181.

Kirkwood, D. S. (1992), Stability of solutions of nutrient salts during storage, *Mar. Chem.*, *38*, 151–164.

Klemas, V., and X. H. Yan (2014), Subsurface and deeper ocean remote sensing from satellites: An overview and new results, *Prog. Oceanogr.*, *122*, 1–9.

Kloosterziel, R. C., G. F. Carnevale, and P. Orlandi (2007), Inertial instability in rotating and stratified fluids: Barotropic vortices, *J. Fluid Mech.*, *583*, 379–412.

Krahmann, G., and F. Schott (1998), Long-term increases in western Mediterranean salinities and temperatures: Anthropogenic and climatic sources, *Geophys. Res. Lett.*, *25*, 4209–4212.

Kunze, E., R. W. Schmitt, and J. M. Toole (1995), The energy balance in a warm-core ring's near-inertial critical layer, *J. Phys. Oceanogr.*, *25*, 942–957.

Lachkar, Z., S. Smith, M. Levy, and O. Pauluis (2016), Eddies reduce denitrification and compress habitats in the Arabian Sea, *Geophys. Res. Lett.*, *43*, 9148–9156, doi:10.1002/2016GL069876.

Lavigne, H., F. D'Ortenzio, H. Claustre, and A. Poteau (2012), Towards a merged satellite and in situ fluorescence ocean chlorophyll product, *Biogeosciences*, *9*, 2111–2125.

Leaman, K. D., and F. A. Schott (1991), Hydrographic structure of the convection regime in the Gulf of Lions: Winter 1987, *J. Phys. Oceanogr.*, *21*, 575–598.

Legg, S., and J. C. Marshall (1993), A Heton model of the spreading phase of open-ocean deep convection, *J. Phys. Oceanogr.*, *23*, 1040–1056.

Legg, S., J. McWilliams, and J. Gao (1998), Localization of deep ocean convection by a mesoscale eddy, *J. Phys. Oceanogr.*, *28*, 944–970.

Le Traon, P.-Y. (1990), A method for optimal analysis of fields with spatially-variable mean, *J. Geophys. Res.*, *95*, 13543–13547.

Lherminier, P., J.-C. Gascard, and D. Quadfasel (1999), The Greenland Sea in water 1993 and 1994: Preconditioning for deep convection, *Deep Sea Res., Part II*, *46*, 1199–1235.

Lilly, J. M., and P. B. Rhines (2002), Coherent eddies in the Labrador Sea observed from a mooring, *J. Phys. Oceanogr.*, *32*, 585–598.

Löscher, C. R., et al. (2015), Hidden biosphere in an oxygen-deficient Atlantic open-ocean eddy: Future implications of ocean deoxygenation on primary production in the eastern tropical North Atlantic, *Biogeosciences*, *12*, 7482–7482.

Margirier F., et al. (2017) Characterization of convective plumes associated with oceanic deep convection in the Northwestern Mediterranean from high resolution in-situ data collected by gliders, *J. Geophys. Res. Oceans*, doi:10.1002/2016JC012633, in press.

Marshall, J., and F. Schott (1999), Open-ocean convection: Observations, theory, and models, *Rev. Geophys.*, *37*, 1–64.

Martin, J. P., C. M. Lee, C. C. Eriksen, C. Ladd, and N. B. Kachel (2009), Glider observations of kinematics in a Gulf of Alaska eddy, *J. Geophys. Res.*, *114*, C12021, doi:10.1029/2008JC005231.

Mayot, N., F. D'Ortenzio, J. Uitz, B. Gentili, J. Ras, V. Vellucci, M. Golbol, D. Antoine, and H. Claustre (2017a), Influence of the phytoplankton community structure on the spring and annual primary production in the North-Western Mediterranean Sea, *J. Geophys. Res. Oceans*, doi:10.1002/2016JC012668, in press.

Mayot, N., F. D'Ortenzio, V. Taillandier, L. Prieur, O. Pasqueron de Fommervault, H. Claustre, A. Bosse, P. Testor, and P. Conan (2017b), Physical and biogeochemical controls of the phytoplankton blooms in the North-Western Mediterranean Sea: A multiplatform approach over a complete annual cycle (2012-2013 DEWEX experiment), *J. Geophys. Res. Oceans*, doi:10.1002/2016JC012052, in press.

McGillicuddy, D. J., et al. (2007), Eddy/wind interactions stimulate extraordinary mid-ocean plankton blooms, *Science*, *316*, 1021–1026.

McWilliams, J. C. (1985), Submesoscale, coherent vortices in the ocean, *Rev. Geophys.*, *23*, 165–182.

McWilliams, J. C. (1988), Vortex generation through balanced adjustment, *J. Phys. Oceanogr.*, *18*, 1178–1192.

McWilliams, J. C. (2016), Submesoscale currents in the ocean, *Proc. R. Soc. London A*, *472*, doi:10.1098/rspa.2016.0117.

MEDOC-Group (1970), Observation of formation of deep water in the Mediterranean Sea, 1969, *Nature*, *225*, 1037–1040.

Meunier, T., C. Ménesguen, R. Schopp, and S. Le Gentil (2015), Tracer stirring around a Meddy: The formation of layering, *J. Phys. Oceanogr.*, *45*, 407–423.

Millot, C. (1987), The circulation of the Levantine Intermediate Water in the Algerian Basin, *J. Geophys. Res.*, *92*, 8265–8276.

Millot, C. (1999), Circulation in the western Mediterranean Sea, *J. Mar. Syst.*, *20*, 423–442.

Morel, A. (1991), Light and marine photosynthesis: A spectral model with geochemical and climatological implications, *Prog. Oceanogr.*, *26*, 263–306.

Morel, A., and J.-F. Berthon (1989), Surface pigments, algal biomass profiles, and potential production of the euphotic layer: Relationships reinvestigated in view of remote-sensing applications, *Limnol. Oceanogr.*, *34*, 1545–1562.

Morel, A., and S. Maritorena (2001), Bio-optical properties of oceanic waters: A reappraisal, *J. Geophys. Res.*, *106*, 7163–7180.

Moutin, T., and L. Prieur (2012), Influence of anticyclonic eddies on the biogeochemistry from the oligotrophic to the ultraoligotrophic Mediterranean (BOUM cruise), *Biogeosciences*, *9*, 3827–3855.

Nencioli, F., V. S. Kuwahara, T. D. Dickey, Y. M. Rii, and R. R. Bidigare (2008), Physical dynamics and biological implications of a mesoscale eddy in the lee of Hawai'i: Cyclone opal observations during E-Flux III, *Deep Sea Res., Part II*, *55*, 1252–1274.

Nencioli, F., F. d'Ovidio, A. M. Doglioli, and A. A. Petrenko (2013), In situ estimates of submesoscale horizontal eddy diffusivity across an ocean front, *J. Geophys. Res. Oceans*, *118*, 7066–7080, doi:10.1002/2013JC009252.

Okubo, A. (1971), Oceanic diffusion diagrams, *Deep Sea Res. Oceanogr. Abstr.*, *18*, 789–802.

Pelland, N. A., C. C. Eriksen, and C. M. Lee (2013), Subthermocline eddies over the Washington Continental Slope as observed by seagliders, 2003–09, *J. Phys. Oceanogr.*, *43*, 2025–2053.

Penven, P., I. Halo, S. Pous, and L. Marie (2014), Cyclogeostrophic balance in the Mozambique Channel, *J. Geophys. Res. Oceans*, *119*, 1054–1067, doi:10.1002/2013JC009528.

Pingree, R. D., and B. Le Cann (1993), A shallow meddy (a smeddy) from the secondary Mediterranean salinity maximum, *J. Geophys. Res.*, *98*, 169–185.

Prater, M. D., and T. B. Sanford (1994), A meddy off Cape-St-Vincent. Part 1: Description, *J. Phys. Oceanogr.*, *24*, 1572–1586.

Provenzale, A. (1999), Transport by coherent barotropic vortices, *Ann. Rev. Fluid Mech.*, *31*, 55–93.

Ras, J., H. Claustre, and J. Uitz (2008), Spatial variability of phytoplankton pigment distributions in the subtropical south pacific ocean: Comparison between in situ and predicted data, *Biogeosciences*, *5*, 353–369.

Rhines, P. B., and W. R. Young (1983), How rapidly is a passive scalar mixed within closed streamlines?, *J. Fluid Mech.*, *133*, 133–145.

Schott, F., and K. D. Leaman (1991), Observations with moored acoustic Doppler current profilers in the convection regime in the Golfe du Lion, *J. Phys. Oceanogr.*, *21*, 558–574.

Schroeder, K., J. Chiggiato, H. L. Bryden, M. Borghini, and S. Ben Ismail (2016), Abrupt climate shift in the western Mediterranean Sea, *Sci. Rep.*, *6*, 23009.

Send, U., J. Font, and C. Mertens (1996), Recent observation indicates convection's role in deep water circulation, *Eos Trans. AGU*, *77*, 61–65.

Sheen, K. L., J. A. Brearley, A. C. Naveira Garabato, D. A. Smeed, L. S. Laurent, M. P. Meredith, A. M. Thurnherr, and S. N. Waterman (2015), Modification of turbulent dissipation rates by a deep southern ocean eddy, *Geophys. Res. Lett.*, *42*, 3450–3457, doi:10.1002/2015GL063216.

Somot, S., F. Sevault, and M. Déqué (2006), Transient climate change scenario simulation of the Mediterranean Sea for the twenty-first century using a high-resolution ocean circulation model, *Clim. Dyn.*, *27*, 851–879.

Testor, P. (2013), DEWEX-MERMEX 2013 LEG1 cruise, RV Le Suroît, technical report, doi:10.17600/13020010.

Testor, P., and J.-C. Gascard (2003), Large-scale spreading of deep waters in the western Mediterranean Sea by submesoscale coherent eddies, *J. Phys. Oceanogr.*, *33*, 75–87.

Testor, P., and J.-C. C. Gascard (2006), Post-convection spreading phase in the northwestern Mediterranean Sea, *Deep Sea Res., Part I*, *53*, 869–893.

Testor, P., et al. (2010), Gliders as a component of future observing systems, in *Proceedings of OceanObs'09: Sustained Ocean Observations and Information for Society*, vol. 2, edited by J. Hall, D. E. Harrison, and D. Stammer.

Testor, P., L. Coppola, and L. Mortier (2013), MOOSE-GE 2013 cruise, RV Téthys II, technical report, doi:10.17600/13450110.

Testor, P., et al. (2017), Observation of deep convection in the northwestern Mediterranean Sea during winter 2012–2013, *J. Geophys. Res. Oceans*, doi:10.1002/2016JC012671, in press.

Thierry, V., and H. Bittig (2016), Argo quality control manual for dissolved oxygen concentration, technical report, Argo-BGC, doi:10.13155/46542.

Thomsen, S., T. Kanzow, G. Krahmann, R. J. Greatbatch, M. Dengler, and G. Lavik (2016), The formation of a subsurface anticyclonic eddy in the Peru-Chile undercurrent and its impact on the near-coastal salinity, oxygen, and nutrient distributions, *J. Geophys. Res. Oceans*, *121*, 476–501, doi:10.1002/2015JC010878.

Timmermans, M.-L., J. Toole, R. Krishfield, and P. Winsor (2008), Ice-tethered profiler observations of the double-diffusive staircase in the Canada Basin thermocline, *J. Geophys. Res.*, *113*, C00A02, doi:10.1029/2008JC004829.

Uitz, J., H. Claustre, A. Morel, and S. B. Hooker (2006), Vertical distribution of phytoplankton communities in open ocean: An assessment based on surface chlorophyll, *J. Geophys. Res.*, *111*, C08005, doi:10.1029/2005JC003207.

Uitz, J. U., Y. Huot, F. Bruyant, M. Babin, and H. Claustre (2008), Relating phytoplankton photophysiological properties to community structure on large scales, *Limnol. Oceanogr.*, *53*, 614–630.

Vargas-Yáñez, M., et al. (2012), Extreme western intermediate water formation in winter 2010, *J. Mar. Syst.*, *105–108*, 52–59.

Vidussi, F., H. Claustre, B. B. Manca, A. Luchetta, and J.-C. Marty (2001), Phytoplankton pigment distribution in relation to upper thermocline circulation in the eastern Mediterranean sea during winter, *J. Geophys. Res.*, *106*, 19,939–19,956.

Visbeck, M. (2002), Deep velocity profiling using lowered acoustic Doppler current profilers: Bottom track and inverse solutions, *J. Atmos. Oceanic Technol.*, *19*, 794–807.

Visbeck, M., J. Marshall, and H. Jones (1996), Dynamics of isolated convective regions in the ocean, *J. Phys. Oceanogr*, *26*, 1721–1734.

Waite, A. M., L. Stemmann, L. Guidi, P. H. R. Calil, A. M. Hogg, M. Feng, P. A. Thompson, M. Picheral, and G. Gorsky (2016), The wineglass effect shapes particle export to the deep ocean in mesoscale eddies, *Geophys. Res. Lett.*, *43*, 9791–9800, doi:10.1002/2015GL066463.

Xing, X., H. Claustre, S. Blain, F. d'Ortenzio, D. Antoine, J. Ras, and C. Guinet (2012), Quenching correction for in vivo chlorophyll fluorescence acquired by autonomous platforms: A case study with instrumented elephant seals in the Kerguelen region (Southern Ocean), *Limnol. Oceanogr.*, *10*, 483–495.